η and η' meson production in the quasi-free proton-neutron collisions at the COSY–11 facility

Rafał Czyżykiewicz

June 2002

.

Abstract

η and η' meson production in the quasi-free proton-neutron collisions at the COSY-11 facility

Both, the structure of the η' meson as well as its production mechanism are still under strong discussion and debate. The most possible hypothesis concerning the explanation of the almost three times larger mass for this meson observed experimentally relative to the theoretically calculated mass is a gluonium admixture to the η' wave function. This gluonium admixture should reflect itself in the production yield of the η' meson in proton-neutron collisions. Since the production of η' meson through the gluonium exchange is isospin independent, the ratio $R_\eta = \frac{\sigma(pn \to pn\eta)}{\sigma(pp \to pp\eta)}$ close to threshold is expected to be $R_\eta = 1$, after corrections for initial and final state interactions.

The close to threshold η' production in proton-proton collisions has already been investigated at the COSY-11 facility. Cross section values in the threshold region have been measured. However, until now no data have been taken for the η' meson production in the proton-neutron collision.

In order to investigate the η' production in proton-neutron collisions at the COSY synchrotron, the COSY-11 facility has been equipped with two new subsystems, namely the neutron detector and the spectator counter. The optimization of the topography for these additional detectors, the selection of the most suitable beam momentum and a discussion for the method of luminosity determination for the quasi-free $pn \to pn\eta(\eta')$ reactions are presented in this thesis. Rates for the production of η and η' mesons in proton-neutron collisions at COSY-11 have been estimated. For the calculations a special fast program has been written.

Contents

1. Introduction

Preparation of experiments described in this thesis aim to investigate the still unexplained structure of the η' meson[1] and the mechanism of its production. The observed mass of this meson is about 3 times larger than it is predicted by the quark model (see. appendix A). The most popular explanation of this effect is a gluonium admixture in the η' wave function that gives additional rise to the meson mass. However, this hypothesis has not been proved yet, and similarly the mechanism of the η' production in the $NN \to NN\eta'$ reaction is not fully understood. According to recent theoretical considerations [1, 2, 3] a measurement of the $pn \to pn\eta'$ reaction should shed light on both, the understanding of the production mechanism of this meson in the nucleon-nucleon interaction and the explanation of its exotic structure. Investigations of the above issues constitute the main motivation for the preparation of the experiments described in this thesis.

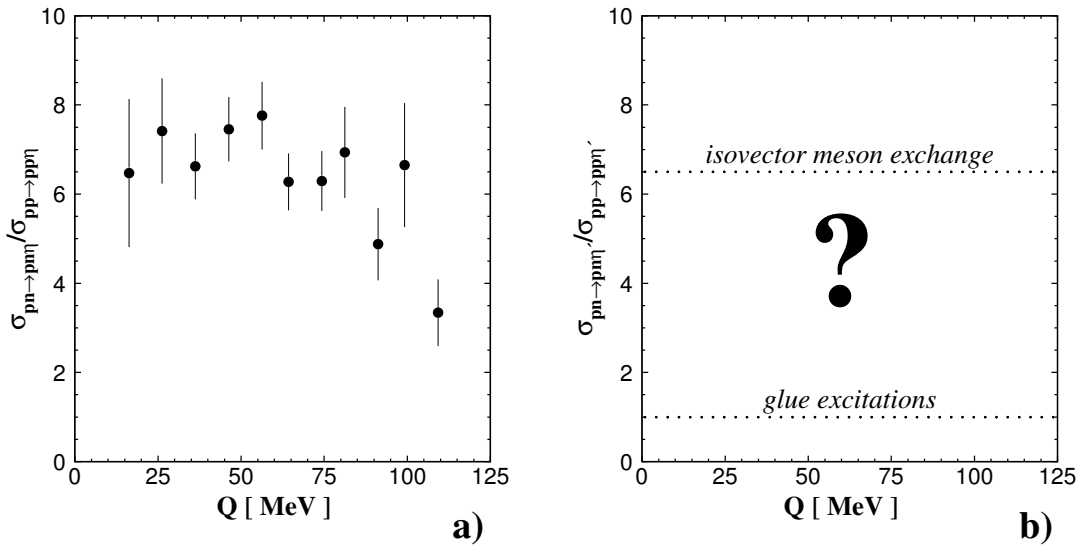

Figure 1.1: (a) $R_\eta = \frac{\sigma(pn\to pn\eta)}{\sigma(pp\to pp\eta)}$ ratio close to threshold. Original data taken from [4]. (b) By now the $R_{\eta'}$ ratio remains unknown, due to the lack of $pn \to pn\eta'$ data.

In the case of η meson production the total cross section has already been measured in both the proton-proton as well as the proton-neutron reactions. The ratio

[1]The η' meson was discovered in 1964 independently by G.R. Kalbfleish and M. Goldberg via the $K^- p \to \Lambda\eta'$ reaction [5, 6]

$$R_\eta = \frac{\sigma(pn \to pn\eta)}{\sigma(pp \to pp\eta)} \tag{1.1}$$

was determined to be about 6.5 **[4] in the excess energy range between** 16 **MeV and** 109 **MeV as depicted in fig. 1.1.a, which reveales a strong isospin dependence of the production process. Since**

$$\sigma(pn \to pn\eta) = \frac{\sigma_{I=0} + \sigma_{I=1}}{2},$$
$$\sigma(pp \to pp\eta) = \sigma_{I=1}, \tag{1.2}$$

we have:

$$\sigma_{I=0} = (2R_\eta - 1)\sigma_{I=1}, \tag{1.3}$$

where I **denotes the total isospin of the nucleon pair. Thus, using the experimental value of** $R_\eta = 6.5$**, the production of the** η **meson with the total isospin** $I = 0$ **exceeds the production with the isospin** $I = 1$ **by a factor of** 12**. This large difference between the total cross sections for these isospin channels can be explained by assuming that the dominant mechanism in the** η **meson production is the one shown in fig 1.2.a (isovector —** π **and** ρ **— meson exchange) [7]. Additionally, angular distributions of the produced** η **meson [8] allowed to conclude that out of** π **and** ρ **meson exchanges,** ρ **is the dominant one [7].**

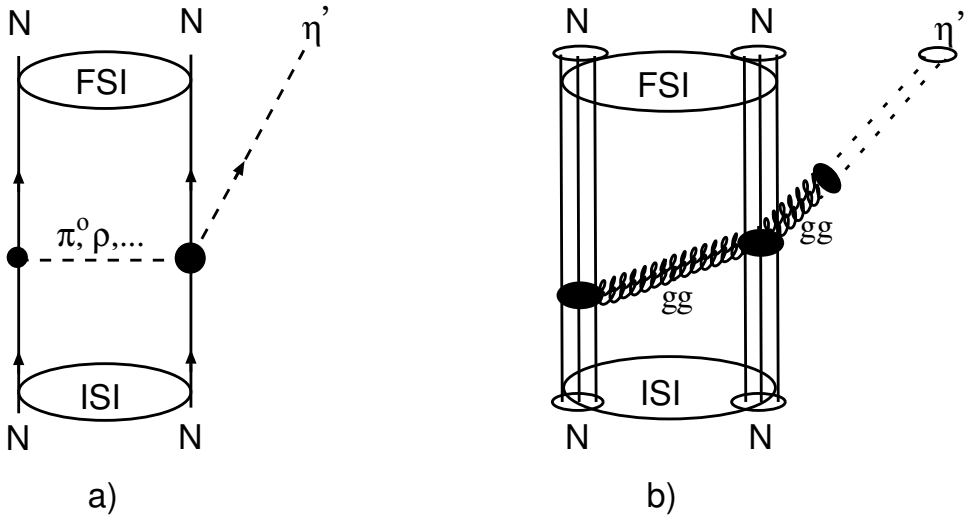

Figure 1.2: $NN \to NN\eta(\eta')$ **close to threshold production. As an example Feynman diagrams for two possible processes are shown: (a) exchange of isovector mesons, (b) production via a rescattering of a "low energy pomeron". Graph (a) is an example of the isospin-dependent mechanism, whereas graph (b) does not depend on the isospin. Figure taken from [9].**

Until now there is no experimental data for the production of the η' **meson in the** $pn \to pn\eta'$ **reaction, thus it is impossible to calculate the** $R_{\eta'}$ **ratio. Provided**

this ratio is known, a similar procedure based on the comparison of the η' production to the channels with isospins $I = 0$ and $I = 1$ together with the knowledge of the angular distribution of η' production will allow to infer about the production mechanism of the η' meson. That is the reason why measurements of the $R_{\eta'}$ ratio are so important. If this ratio appears to be close to the R_η ratio, it would mean that isovector meson exchange mechanism is dominant in η' production. If this value is close to unity after corrections for final and initial state interaction between the participating baryons, this would mean that the η' meson is produced by an isospin independent mechanism, e.g. via rescattering of a glueball excited in the interaction region [1] (fig. 1.2.b).

Experiments described in this thesis will be performed by the COSY-11 collaboration[2] at the COSY accelerator and storage ring [10] in the Research Centre Jülich (FZ-Jülich[3]), Germany. A first run of the experiment will take place in June 2002. Measurements will provide information on the properties of meson production close to threshold. The main goal of this thesis was to find out the best conditions for measuring quasi-free $pn \to pn\eta(\eta')$ reactions, in particular to optimize the configuration of the detection system and to determine the optimum beam momentum.

Chapter 2 of this work introduces quasi-free meson production and basic problems connected with this method which mainly come from the fact that the neutron on which proton scattering takes place is not a free particle, but is bound inside the deuteron. At the end of this section some nuclear effects that have influence upon the reduction of beam flux are described.

In Chapter 3 the experimental setup is presented with the special emphasis put on two new experimental subsystems at COSY-11, namely the spectator – and the neutron detector. Mounting of these two new detector subsystems at the COSY-11 facility requires a determination of their position. Moreover, due to the Fermi motion of nucleons inside the deuteron the optimum beam momentum should be selected. The main point of this chapter is the optimization of i) the beam momentum and ii) the configuration of the detectors. The beam momentum has been found with an accuracy of 5 MeV/c as well as the spectator detector's position with an accuracy of 1 mm. Simulations have been performed by means of a special programme written for this purpose described in details in Appendix C.

[2]COSY-11 is an international group involving several European institutes and universities: Nuclear Physics Institute, Research Center Jülich; Zentrallabor für Elektronik, Research Center Jülich; Nuclear Physics Institute, Westfälische Wilhelms-Universität Münster; Institute of Physics, Jagellonian University of Cracow; Institute of Nuclear Physics, Cracow; Institute of Physics, University of Silesia, Katowice.

[3]FZ-Jülich official web site - www.fz-juelich.de

Methods of the luminosity determination via proton-deuteron elastic scattering together with a short description of the background for the luminosity measurements, mainly from the proton-proton quasi-free scattering, are described in Chapter 4.

Simulation results are presented in Chapter 5.

In Chapter 6 a summary is given. Some possibilities of extending the experiments described in this thesis are pointed out.

Three appendices have been added. The problem of the η' mass is presented in Appendix A. Appendix B comprises a brief description of deuteron wave functions of Paris and CD-Bonn potential models that were used to obtain the momentum distribution of a neutron inside a deuteron. Finally, in Appendix C a general description of the simulation programme written to generate results presented in this thesis is included. It should be noted that this simulation programme makes up an important part of this thesis. The source of the programme is available from the author [4].

[4]E-mail address: czyzyk@pisa.if.uj.edu.pl

2. Quasi-free meson production

2.1 Proton scattering on the neutron bound inside the deuteron

Since pure neutron targets are not available, either neutron beams, produced in proton collisions with light nuclei [11] or deuteron targets are usually used in order to investigate meson production in proton-neutron collisions.

A good energy resolution of the beam may be realized only with a cooled proton beam. Therefore, the latter of the above mentioned possibilities will be used at the COSY-11 facility. A cooled proton beam together with an internal windowless deuteron cluster target will be applied for this purpose. A similar method has been previously used by the WASA/PROMICE collaboration at the CELSIUS accelerator in Uppsala in the production of π^0 and η mesons in proton-neutron collisions [12, 13]. There were no experiments performed until now that would have measured η' meson production in p-n collisions.

Total cross sections for the $pd \rightarrow pnp_{sp}\eta'(\eta)$ reaction are going to be measured by COSY-11 collaboration in June 2002 at the COSY storage ring in the Forschungszentrum Jülich, Germany. The method of the measurement together with a description of the COSY-11 detection setup is given in section 3.1. In order to identify a meson produced in quasi-free proton neutron scattering it is necessary to measure either the decay products of this meson or to register all outgoing nucleons (nuclei). At the COSY-11 facility the latter possibility will be realized, where the mesons created in these reactions will be identified via the missing mass method. This requires the knowledge of four momenta of all incoming and outgoing nucleons. The method used for measurement of all these quantities is presented in section 3.1. One can calculate the missing mass (m_x) of an undetected particle or system of particles in the exit channel knowing all needed nucleon four-momenta:

$$m_x^2 = E_x^2 - \vec{p}_x{}^2 = (P_b + P_t^n - P_p - P_n)^2 = \\ = (E_b + E_t^n - E_p - E_n)^2 - (\vec{p}_b + \vec{p}_t^{\,n} - \vec{p}_p - \vec{p}_n)^2. \tag{2.1}$$

In the above equation following notations have been used:
$P_b = (E_b, \vec{p}_b)$ **— four-momentum vector of the beam proton,**
$P_t^n = (E_t^n, \vec{p}_t{}^n)$ **— four-momentum vector of the target neutron,**
$P_p = (E_p, \vec{p}_p)$ **— four-momentum vector of the outgoing proton**
$P_n = (E_n, \vec{p}_n)$ **— four-momentum vector of the outgoing neutron.**

The square of the total energy in the center-of-mass system is a Lorentz invariant:

$$(E^*_{tot})^2 = s = (P_p + P_n)^2 = (E^*_p + E^*_n)^2 = (Q + \sum_i m_i)^2, \tag{2.2}$$

where E^*_{tot}, E^*_p, E^*_n are the energies in centre-of-mass system — total, proton and neutron respectively, and Q denotes the excess energy, i.e. center-of-mass kinetic energy shared among the outgoing particles. The summation is over all initially produced particles masses.

In order to compare the dynamics of the η and η' meson production via the $pn \to pnX$ reaction it is convenient to express the total cross section as a function of the excess energy Q. The derivation of this quantity from equation 2.2 gives:

$$Q = \sqrt{s} - \sum_i m_i. \tag{2.3}$$

The four-momentum vectors of the exit particles of the $pn \to pnX$ reaction will be identified utilizing the COSY-11 detection system, and the momentum of the synchrotron beam will be determined from the frequency measurement and the known beam optics. Thus, the only unknown quantity for deriving the excess energy is the target's neutron four-momentum. Its direct measurement prior to the reaction itself is impossible due to the Fermi motion of the nucleons inside a deuteron. However, in the frame of the impulse approximation it can be derived from the measurement of the spectator proton momentum as will be described in the next section.

2.2 Impulse approximation

The small deuteron binding energy ($E_B = 2.2 MeV$) relative to the kinetic energy of beam protons (which is about 1335 MeV for η production and about 2530 MeV for η' production) allows to consider the neutron taking part in the reaction as a free particle in the sense that the matrix element for the quasi-free meson production on a bound neutron is equal to the one for the free reaction [9]. In this so called impulse approximation the proton from the deuteron is considered as a spectator which leaves the interaction region undisturbed, carrying only the Fermi momentum posessed at the moment of collision. Previous measurements performed at CELSIUS [4, 14] and TRIUMF [15, 16] have proven that the offshellness of the reacting neutron can be neglected and that the spectator proton influences the interaction only in terms of the associated Fermi motion [9]. As an example the total cross sections for the free and quasi-free $pp \to pp\eta$ reactions are shown in fig. 2.1.

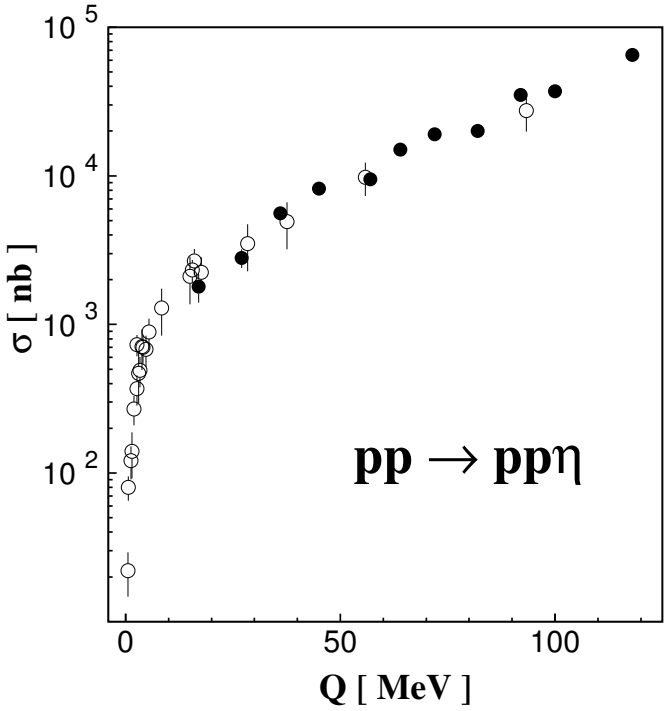

Figure 2.1: Total cross sections for the $pp \to pp\eta$ reaction as a function of excess energy for free (open circles) and the quasi-free scattering of protons (full circles). Figure copied from [17].

Using the notation from equation 2.1, the discussed approximation can be expressed via the following relation:

$$P_b + (P_{sp} + P_t^n) = P_n + P_p + P_{sp} + P_X, \tag{2.4}$$

where additionally spectator (P_{sp}) and meson (P_X) four-momenta have been introduced.

The spectator proton is a real particle registered in the experiment, therefore it is on its mass-shell:

$$|P_{sp}|^2 = m_p^2. \tag{2.5}$$

Additionally for the deuteron we have:

$$|P_{sp} + P_t^n|^2 = m_d^2, \tag{2.6}$$

where m_d denotes the deuteron mass and equals to $m_d = 1875.6$ MeV/c^2 [18]. In the deuteron centre-of-mass frame:

$$\vec{p}_n = -\vec{p}_{sp}, \tag{2.7}$$

thus 2.6 and 2.7 give together:

$$E_n = m_d - E_{sp}, \tag{2.8}$$

Therefore in this approximation measuring the momentum vector of the spectator proton (as will be described in section 3.1) and taking into account relations 2.7 and 2.8 one can deduce the neutron four-momentum vector at the moment of reaction and furthermore using equation 2.3 one can calculate the excess energy Q for each event.

The measurements of the spectator four-momentum at COSY-11 will be performed by means of the silicon detector, described in 3.2.1–3.2.2.

2.3 Nucleon momentum distribution inside a deuteron

Due to the Fermi motion, the neutron bound inside a deuteron is not at rest but moves with a momentum which varies in a rather broad range. The momentum distributions of nucleons inside the deuteron derived from two different potential models, namely PARIS [19] and CD-BONN [20] potentials, are presented in fig. 2.2.

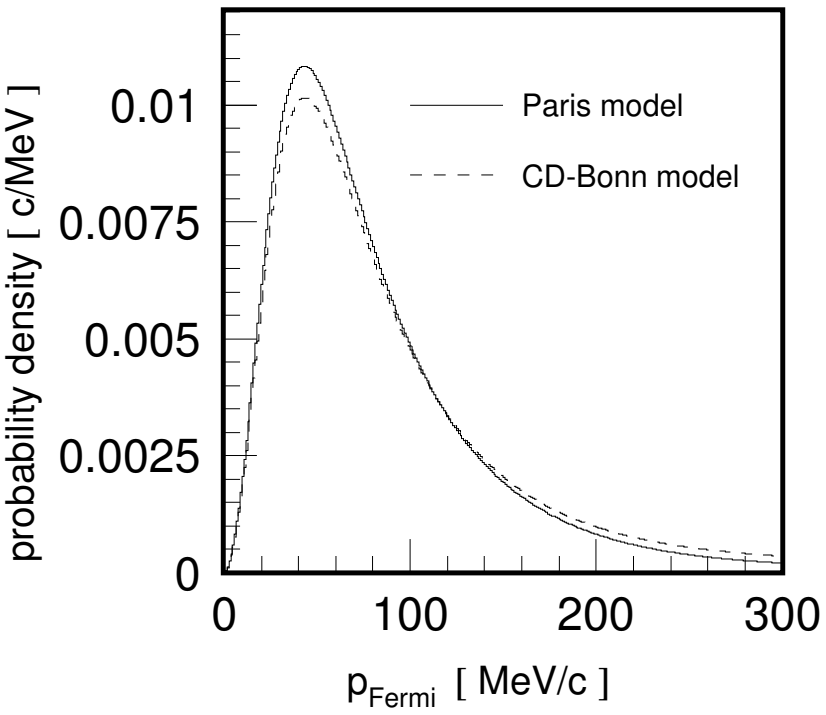

Figure 2.2: Momentum distribution of nucleons inside the deuteron for Paris (full line) and CD-Bonn (dotted line) potentials. For more details see Appendix B.

Fermi momentum distributions are peaked at about 40 MeV/c but due to the long tail of the distribution the mean momentum ($< p^2 >$) is approximately equal to 100 MeV/c. The variation of the neutron momentum influences the distribution of the excess energy Q in the centre-of-mass system. Therefore Q is not a fixed value but varies from event to event for a constant beam momentum as depicted in fig. 2.3. This is similar to using a proton beam with an energy spread of the order of $\sigma = 100$ MeV [13].

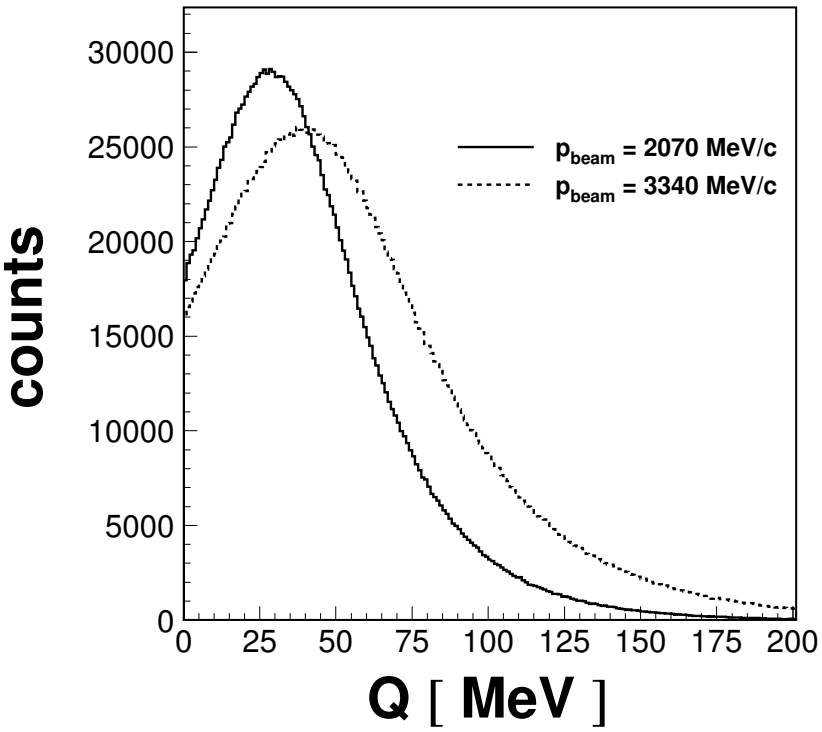

Figure 2.3: Distribution of the excess energy Q in the centre-of-mass system for the η meson production at the proton beam momentum of 2070 MeV (full line) and for the η' production at the proton beam momentum of 3340 MeV (dotted line).

Thus the variation of the neutron momentum allows measurements of the total cross sections for different excess energy values at one fixed proton beam momentum.

The total cross section strongly depends on the excess energy close to the reaction threshold. It varies by more than two orders of magnitude in the excess energy range of few tens of MeV as can be seen in fig. 2.1. In order to achieve a high quality measurement of the cross section, the excess energy Q has to be

known with a high accuracy for each event. Apart from the error of the Q value arising mainly from the angular and energy resolution of the spectator detector one has to take into account a systematic error which originates from the choice of the deuteron wave function parametrization. Estimation of the systematic uncertainity of observables was performed by means of Monte-Carlo simulations of the quasi-free $pn \to pn\eta'$ reaction. In the simulations Paris and CD-Bonn deuteron wave function models have been used. Momentum distributions for particles inside the deuteron for both mentioned wave function parametrizations are presented in fig. 2.2. In the experiment only spectators with total momenta up to 130 MeV/c will be registered [9]. In this momentum range the Fermi momentum distributions deduced from Paris and CD-Bonn potentials differ no more than by 5.4 % [21]. The resulting systematic error in the determination of the total cross section energy dependence originating from the choice of the deuteron potential is expected to be of the same order.

2.4 Shadowing and reabsorption

The quasi-free meson production is disturbed by some nuclear effects which originate from the presence of the spectator proton. The, so called shadow effect, which is simply a reduction of the beam flux on the neutron, originating in neutron shielding by a spectator proton decreases the total cross section by about 4.5 % in the case of η production [22]. However the same effect will also reduce the cross section of quasi-elastic scattering which is used to normalise the $\eta(\eta')$ production, therefore this effect will cancel itself to some extent and it is not necessary to take it into account in extracting the cross section.

The second important effect we deal with in the quasi-free meson production is the reabsorption of the produced meson by the spectator proton. Reabsorption is proportional to the average of the inverse square of the distance between two nucleons in the deuteron. Chiavassa et al. [22] estimated this effect to reduce the cross section by a factor of $2-4$ % for the η production, depending on the energy of the η meson. Thus this effect is rather small. It is even smaller when considering the reabsorption of the produced η' due to the weak $p-\eta'$ interaction [23].

3. Experimental method

3.1 COSY-11 detection setup

Measurements of $pd \rightarrow pnp_{sp}\eta(\eta')$ reactions will be performed by means of the COSY-11 detection setup [24], which is schematically depicted in fig. 3.1.

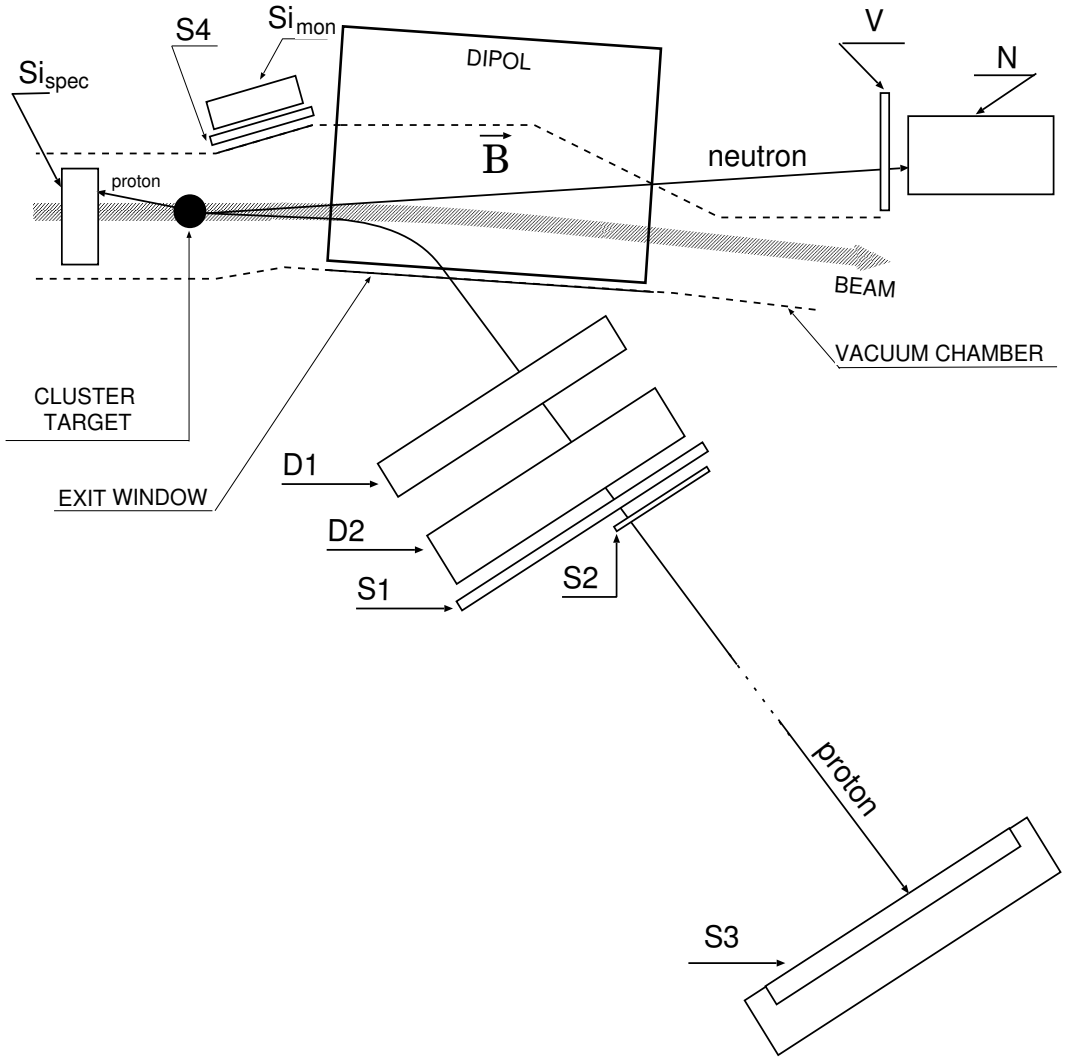

Figure 3.1: Schematic view of the COSY-11 detection setup [24]. Only detectors needed for the measurements of the $pd \rightarrow pnp_{sp}\eta(\eta')$ reaction are shown. D1 and D2 denotes the drift chambers; S1-S4 and V represent scintillation detectors; Si_{mon} and Si_{spec} silicon detectors for measurements of the elastic scattering and spectator protons respectively; N stands for neutron detector. Picture taken from [9].

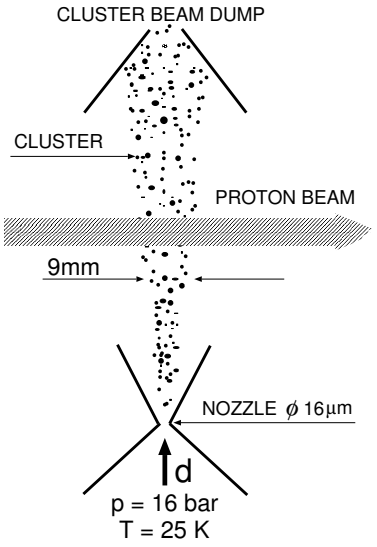

Figure 3.2: Schematic view of the COSY-11 cluster target. Figure taken from [27].

A deuterium cluster target (fig. 3.2) having a density of about $5 \cdot 10^{13}$ atoms/cm^2 is installed in front of one of the dipole magnets. Every single cluster contains about 10^4 atoms. Over 10^{10} accelerated protons pass through the deuterium cluster target about $1.6 \cdot 10^6$ times per second. Mesons can be produced at the intersection points of cluster beam with the COSY proton beam[1] in the collisions schematically depicted in fig. 3.3.

Due to the large beam momentum, reaction products are moving forward and reach the region with the magnetic field induced by a magnet shown schematically in fig. 3.1. Since the reaction products have smaller momenta than beam protons, trajectories of the charged products are bent more in the magnetic field of the dipole magnet. They leave the scattering chamber through the thin exit foil [24], whereas beam protons remain on their orbits inside the ring. Protons from the $pd \rightarrow pnp_{sp}\eta(\eta')$ reactions having bent their trajectories in the magnetic field reach the detection subsystems such as drift chambers D1 and D2 [24, 27], scintillation hodoscopes S1 and S2 [24, 27] and the scintillation wall S3 [24, 27]. Neutrons, which move forward are registered by the neutron detector, which will be described in section 3.3. Spectator protons are measured by means of the spectator detector presented in the next section.

Aside from the $pd \rightarrow pnp_{sp}\eta(\eta')$ reactions, the proton-deuteron elastic scattering as well as the proton-proton quasi-free scattering measurements are going to be performed in order to obtain the information on the luminosity. Silicon pad monitors [27, 24] are the additional detector subsystems used for measuring this

[1]Cluster target's smearing is about 9 mm in diameter [25], whereas the beam's smearing differs in both horizontal and vertical dimensions and equals 0.2 cm and 0.4 cm respectively (standard deviations) [26].

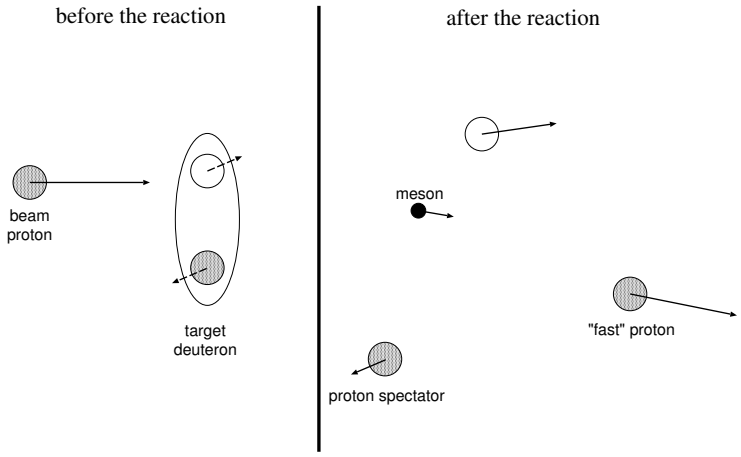

Figure 3.3: Schematic picture of the quasi-free meson production. Short dotted arrows represent the Fermi momenta of the nucleons inside the deuteron. Protons are depicted as shaded circles whereas neutrons are represented by the open circles.

kind of reactions. A method of obtaining the luminosity is described in chapter 4.1.

Tracing the trajectories of particles inside the drift chambers back to the target position with a well known magnetic field of the dipole magnet allows to reconstruct the momentum vector for each particle that gave signals inside the drift chambers. A special programme [28] is used for reconstruction of the particle's track inside the drift chambers and for evaluation of particle's momentum vector. The time of flight measured between S1 and S3 or (S2 and S3) allows to determine the particle's velocity. Knowing the particle's velocity and its momentum vector one can calculate its mass and identify it. After the particle has been identified, tracking back its momentum vector to the target point provides the time of the reaction at the target.

The angle defined by the centre of the hit segment inside the neutron detector will allow to deduce information about the direction of the neutron momentum vector, whereas its absolute value will be calculated from the time of flight measurement between the target and the neutron detector.

Similarly, the angle defined by the centre of the hit segment inside the spectator detector (see 3.2.1) will serve for determining the angle of the spectator proton. It's kinetic energy (T_{sp}) will be directly measured as the energy loss in silicon (providing that the spectator will be stopped in the first silicon layer — see 3.2.1). With the spectator's energy known one can calculate its momentum value:

$$|\vec{p}_{sp}| = \sqrt{(T_{sp} + m_p)^2 - m_p^2}, \tag{3.1}$$

where m_p stands for the proton mass. Thus we have the spectator proton four momentum — $P_{sp} = (E_{sp}, \vec{p}_{sp})$. Taking into account relations 2.8 — 2.7 and the impulse approximation (section 2.2) one can calculate the target neutron four mo-

mentum at the moment of reaction:

$$P_n = (m_d - T_{sp} - m_p, -\vec{p}_{sp}). \tag{3.2}$$

Since the four-momentum of the beam proton is known, one has all quantities required for calculations of the excess energy (eq. 2.3) and the missing mass of the meson (eq. 2.1).

At the end of this section the trigger conditions are outlined. For the $pd \to pnp_{sp}\eta(\eta')$ measurements coincidence signals in the S1 or S2 start counters, S3 stop scintillator and at least one module of the neutron detector will be required. These trigger conditions are written schematically below:

$$T_{\eta,\eta'} = (T_{S1} \vee T_{S2}) \wedge T_{S3} \wedge T_N. \tag{3.3}$$

A requirement of the necessary simultaneous registration of signals in the drift chambers and the spectator detector will be performed in the offline analysis. In particular, only events with more than 12 signals in both drift chambers will be considered.

For the proton-deuteron elastic scattering and for the quasi-free proton-proton scattering we require:

$$T_{p-d} = T_{S1} \wedge T_{S4}, \tag{3.4}$$

and the same statistics of hits in the drift chambers is required.

Since the standard COSY-11 components and COSY-11 Data Acquisition System are well described in many COSY-11 publications and PhD theses [24, 27, 29] I would like to focus only on two new detector subsystems installed at the COSY-11 facility, namely the spectator and neutron detectors.

3.2 Spectator detector

A new silicon detector subsystem has been installed at the COSY-11 facility in order to identify the quasi-free $pd \to pnp_{sp}X$ reactions. This detector will allow to determine the excess energy Q for each registered event. In this section some of the properties of the spectator detector used at COSY-11 will be described.

3.2.1 Scheme of the spectator detector

The spectator detector [12] used at COSY-11 was previously used in the experiments at the CELSIUS storage ring of The Svedberg Laboratory by the PROMICE/WASA collaboration. This detector allows to measure the emission angle and kinetic energy of the spectator proton, which are necessery to determine the Q value.

Four modules as schematicaly depicted in fig. 3.4 form the spectator detector.

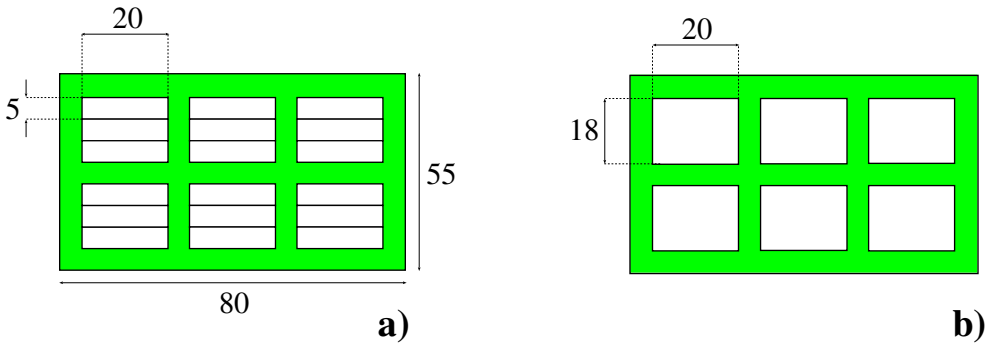

Figure 3.4: Schematic view of the spectator detector's single module: a) front layer (dE), b) back layer (E).

The whole system is placed in a high vacuum at the COSY storage ring as shown in fig. 3.5.

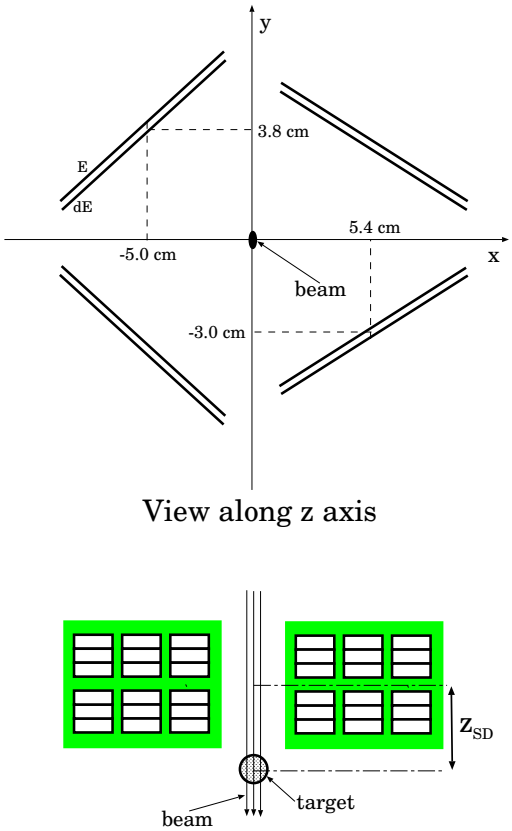

Figure 3.5: Schematic view of the spectator detector as installed at the COSY-11 facility. The z-axis corresponds to the beam direction, x is chosen to be parallel to the acceleration plane.

The location of the modules inside a scattering chamber excludes plastic as an active material. Moreover, a proper identification of the spectator four momentum requires a good energy resolution of the spectator detector. These two restrictions are well satisfied by silicon, which was used as an active material in the spectator detector. In each module there are two layers of silicon, namely front and back layer. The front layer refers to the plane closer to the beam, whereas the back layer is simply a plane which lies further away with respect to the beam. The front layer consists of 18 **silicon strips, each** 300 μ**m thick. The active area of each single strip amounts to** 20 **mm** $\times$ 5 **mm. The back layer of each module is made of** 6 **silicon strips, also of** 300 μ**m thickness, but in this layer the active area of a single strip is larger, namely** 20 **mm** $\times$ 18 **mm** [2]**. The geometry of both layers is shown in fig. 3.4. The back layers of the spectator detector will be used as**

[2]Si-detectors were manufactured by ELMA Research Association[30]. Undoped float-zone n-type 300 μm silicon wafers were produced at Wacker [31].

anticoincidence counters for distinguishing between signals originating from the fast particles[3] and the slow spectator protons which will be stopped in the first layer with a probability of 70 %.

Signals from each of the 96 silicon strips are led by four electronic buses (one bus from each module) towards the scattering chamber's flange, where preamplifiers are placed. In order to protect the beam current from the electromagnetic field generated by the signals, multi-layer Kapton sheets have been used as shown in fig. 3.6. The detector part was equipped with three additional Kapton sheets to provide fixation and rigidity for the head of the modules [12].

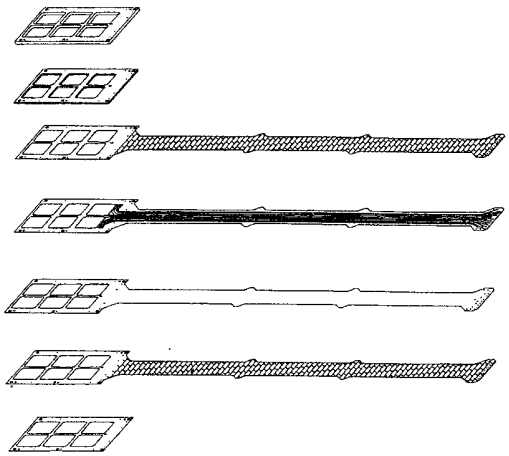

Figure 3.6: Spectator detector - unit module. Individual kapton sheets are shown. Function of the Kapton sheets (from the top to the bottom of the figure): rigidity layers (2 sheets), electromagnetic shield, transmission line, rigidity sheet, electromagnetic shield, rigidity layer. Figure taken from [12].

Tests of the vacuum compatibility were performed at The Svedberg Laboratory for each detector unit. Heating the units at 150^o C for 10 h in a test chamber did not disturb the vacuum. A preasure of $5 \cdot 10^{-9}$ Torr was reached, which was the limit for the chamber itself at the time of the test [12]. The typical high vacuum of the COSY storage ring in the vicinity of the COSY-11 cluster target is about 10^{-8} Torr during experimental runs, therefore the spectator detector is not expected to worsen the experimental conditions at COSY.

3.2.2 Calibration of the spectator detector

At the PROMICE/WASA experiments the minimum energy of the spectators which still could have been identified was about 0.5 MeV [12]. At this value the dis-

[3] A significant part of the background to the $pd \to pnp_{sp}\eta$ reaction as well as to $pd \to pnp_{sp}\eta'$ reaction will be due to registering pions (from pion production channels) by the spectator detector instead of protons.

tribution of the nucleons' kinetic energy inside a deuteron reaches its maximum, as depicted in fig. 3.7.

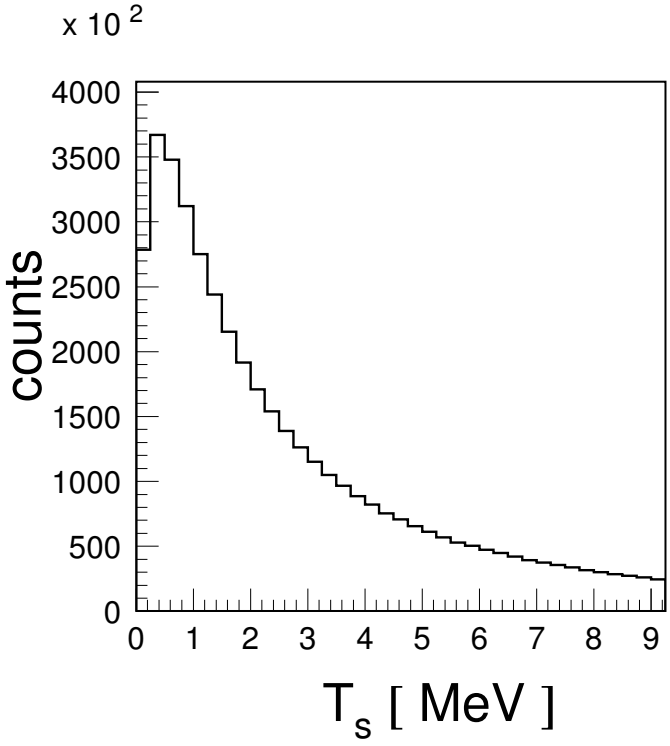

Figure 3.7: Kinetic energy distribution of the nucleons inside the deuteron, generated according to the Paris parametrization of the deuteron wave function [19].

The adoption of the spectator detector to the COSY-11 setup required some changes in the signal conducting system. Transmission lines had to be extended by about 50 cm with respect to those used by the PROMICE/WASA group [4]. The presence of the additional transmission circuit increases the capacity of the detection setup by about 40 %, hence increases the noise and as a consequence reduces the capability of identification of the low energy spectator protons. In order to compensate the growth of the noise level due to the extension of the signal transmitters, the preamplifiers have been modified and the signal to noise ratio was improved by a factor of 2 [32, 33].

Tests of the energy resolution for each of the 96 silicon strips (with short transmission line), were performed in a special prepaired scattering test chamber using

[4]Cable extension have been manufactured by the STRASCHU company [35].

Plutonium, Americium and Curium α-sources. As an example a spectrum obtained for one of the strip is presented in figure 3.8.

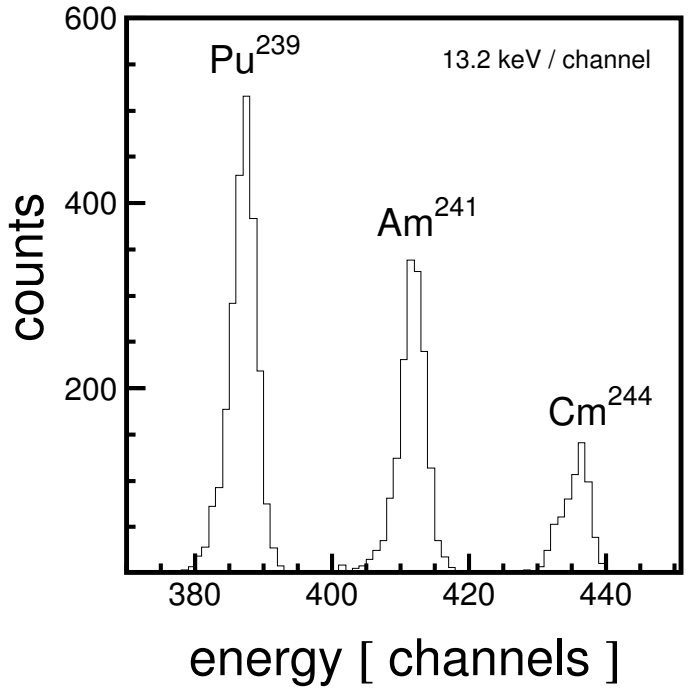

Figure 3.8: Energy spectrum of alpha particles emitted from ^{239}Pu, ^{241}Am and ^{244}Cm with mean kinetic energies of 5.15 MeV, 5.48 MeV and 5.80 MeV, respectively. Figure taken from [34].

As one can see the energy resolution (FWHM) is better than 40 keV. Monte-Carlo calculations for the $pd \to pnp_{sp}\eta'$

reaction with the conservative assumption that the extension of cables and the operation at the COSY ring will decrease the energy resolution to 100 keV lead to an 8 MeV width of the missing mass peak for excess energies lower than 40 MeV as shown in fig. 3.9.

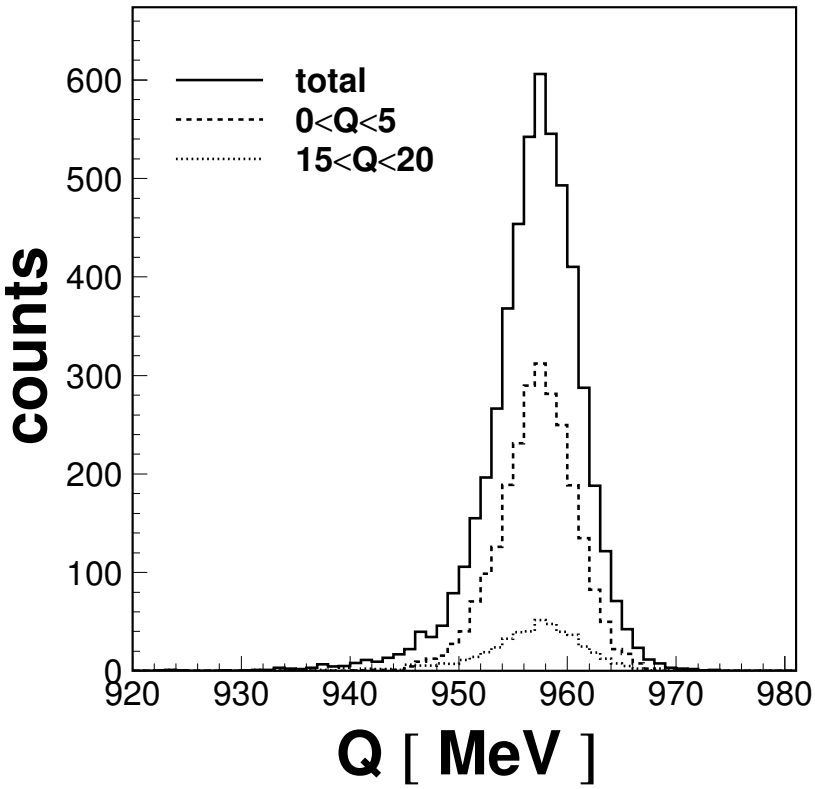

Figure 3.9: Missing mass distribution with respect to the pn subsystem of the quasi-free $pn \to pn\eta'$ reaction as reconstructed from $5 \cdot 10^6$ simulated events. The neutron detector was placed at a distance 730 cm from the target. The spectator detector was positioned at $z_{SD} = -2.8$ cm with the z-axis along the beam direction. The beam momentum was set to be 3340 MeV/c.

3.3 Neutron detector

24 modules, such as the one shown schematically in fig. 3.10, form the neutron detector. The segmentation allows to optimize their arrangement according to the experimental needs. In order to optimize the efficiency and the momentum resolution for the neutron registration two configurations presented schematically in fig. 3.11 have been considered.

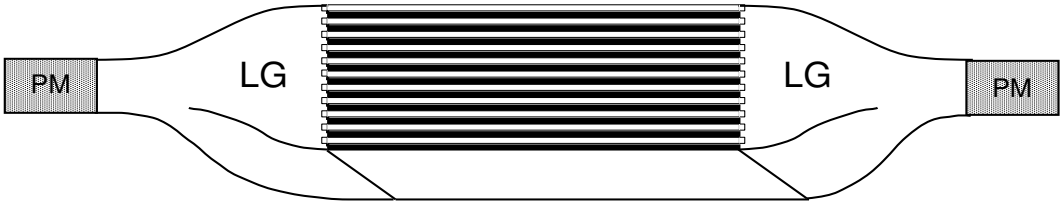

Figure 3.10: Scheme of a neutron detector module. 11 plastic scintillator plates (white layers) are interlayed by the same amount of lead sheets (dark layers). LG and PM denote light guides and photomultipliers, respectively.

Each module is built out of 11 plastic scintillator plates with dimensions of $270 \times 90 \times 4$ mm^3 interlayed by 11 lead plates with the same dimensions (fig. 3.10). The scintillators are read out from both sides by light guides (LG) made of plexiglass, which shapes change smoothly from rectangular into cylindrical. This allows to collect the scintillation light onto a circular (4 cm of diameter) photocathode of a photomultiplier (PM). The photomultiplier changes the light impulse into an electric signal, which is splitted into two branches. After an appropriate delay determined by the trigger setup, they are conducted to analog-to-digital (ADC) and — after discrimination in order to reduce the noise level — to time-to-digital (TDC) converters. Multiplicity outputs of the discriminator modules are used for the corresponding trigger signal.

In the search for the optimum position of the neutron detector, two configurations which cross-sections are schematically depicted in fig 3.11 have been investigated. The upper configuration will be further called a "3×8" configuration, whereas the bottom one will be referred as a "5×5" configuration[5].

[5]Even though there are 24, not 25 modules forming this configuration.

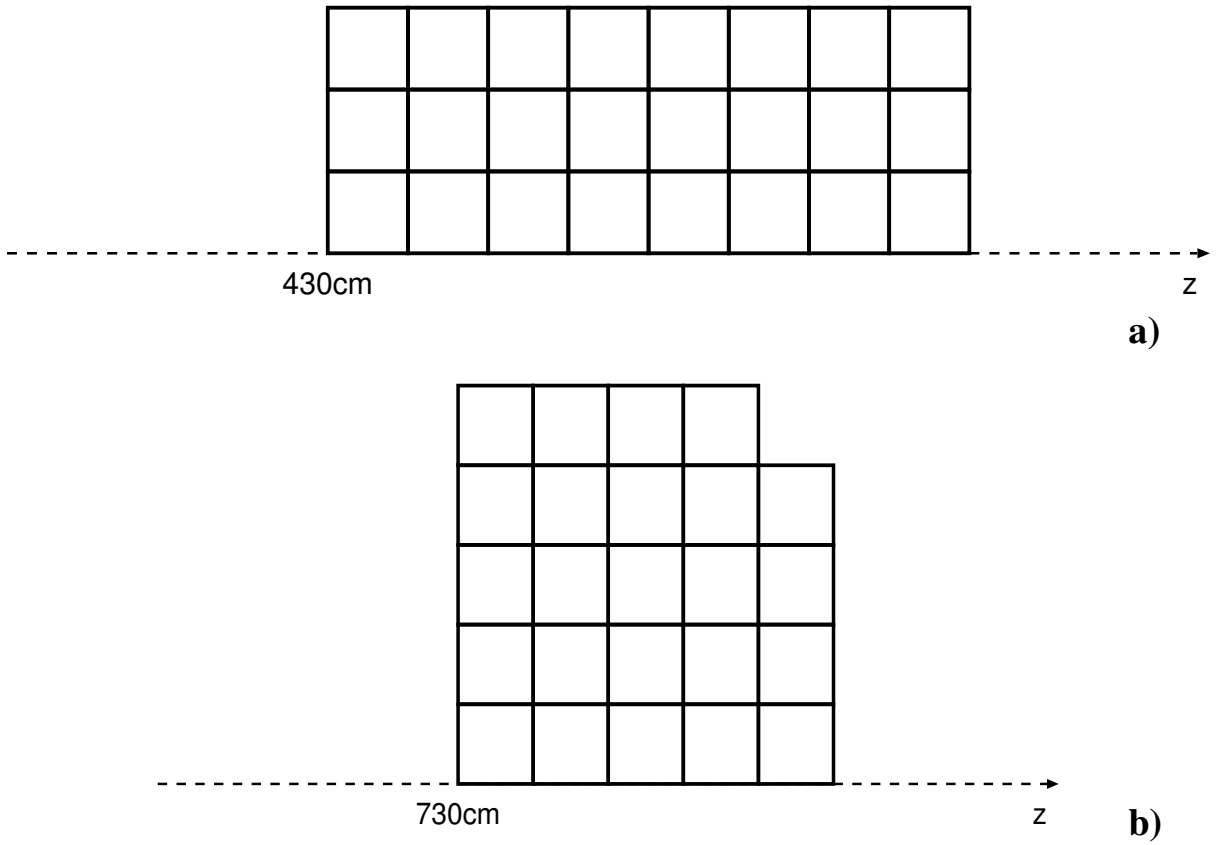

Figure 3.11: Two neutron detector configurations considered for two possible positions at distances of 430 cm and 730 cm from the target along the beam axis. Squares represent individual modules of the neutron detector. z axis is defined by the average momentum vector of the beam protons at the intersection point with the target clusters.

Obviously, between these two configurations there are differences in the geometrical acceptance as well as in the efficiency of the neutron detector. The influence of the neutron detector configuration upon the detection efficiency of the whole detector system will be shown in section 5.4.

4. Luminosity evaluation

The number of all $pd \to pnp_{sp}\eta(\eta')$ reactions taking place at the time t within an interval dt and at the excess energy Q — $\frac{dN}{dt}(t,Q)$ — has to be normalized to the areal density of the target and the number of protons passing through the target within the time interval dt. This normalized value of the reaction rate is called the total cross section and will be further denoted as $\sigma(Q)$. The normalization factor — $L(t)$ — is called luminosity [1]. Thus total cross section can be expressed as [27]:

$$\sigma(Q) = \frac{\frac{dN}{dt}(t,Q)}{L(t) \cdot E_{ff}(Q)} \tag{4.1}$$

where E_{ff} is the detection efficiency.

Taking into account all relevant properties of the detection system the detection efficiency can be evaluated by means of the Monte Carlo method as a ratio of number of "registered" to generated reactions. The number of produced mesons during the total time T of the experiment ($N_{int} = \int_{t=0}^{T} \frac{dN}{dt}(t,Q)dt$) and the luminosity ($L_{int} = \int_{t=0}^{T} L(t)dt$) will be determined experimentally. The luminosity will be controlled by the measurement of a reaction with known cross section. Afterwards the cross section will be calculated as:

$$\sigma(Q) = \frac{N_{int}}{L_{int} \cdot E_{ff}(Q)}. \tag{4.2}$$

Two possible reactions which can be used for the determination of the luminosity will be discussed in the next sections.

4.1 Proton-deuteron elastic scattering

The determination of the luminosity for $pd \to pnp_{sp}\eta(\eta')$ reactions will be performed from simultaneous measurement of proton-deuteron elastic scattering. Similar to equation 4.1 the centre-of-mass differential cross section $\frac{d\sigma^*}{d\Omega^*}$ for the proton-deuteron elastic scattering can be expressed as [27]:

$$\frac{d\sigma^*}{d\Omega^*}(\theta_2^*) = \frac{1}{L_{int}} \cdot \frac{\Delta N(\theta_2^*)}{\Delta\Omega^*(\theta_2^*)} \tag{4.3}$$

where $\Delta N(\theta_2^*)$ is a number of protons elastically scattered in the solid angle $\Delta\Omega^*$ around the centre-of-mass angle θ_2^* corresponding to the laboratory angle θ_2 shown in fig. 4.1.

[1] Luminosity is a function of time since the target's density is not always the same due to irregular flow of gas through the target's nozzle. Number of protons circulating inside the ring decreases within the period of one cycle, which also contributes to the luminosity variation within this time.

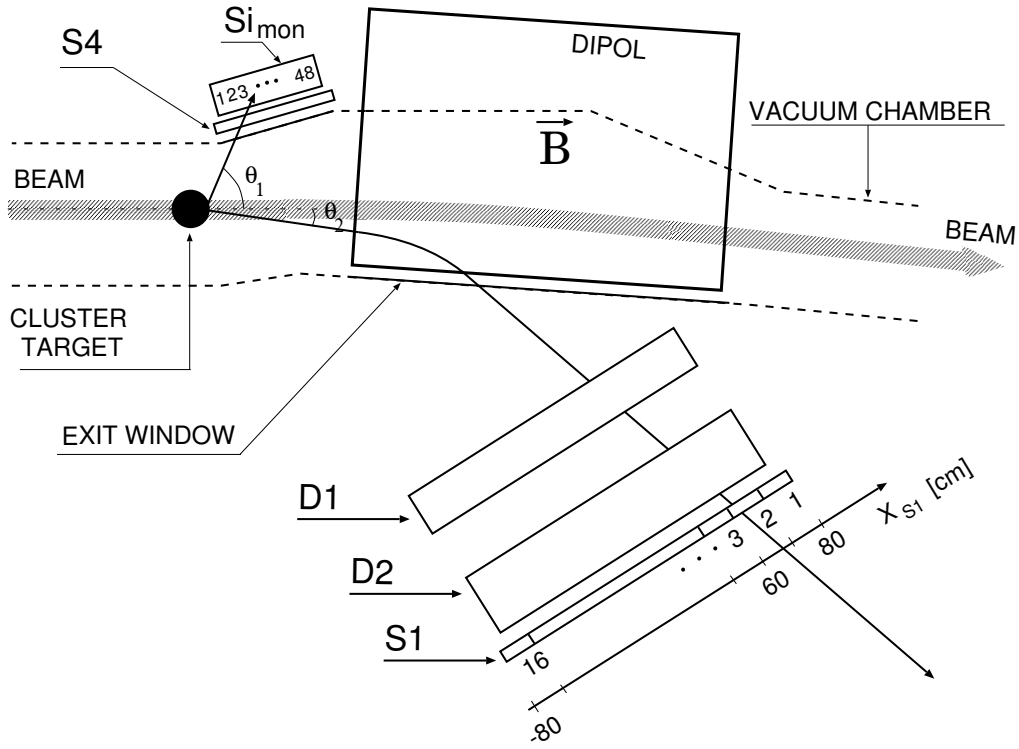

Figure 4.1: Schematic view of the COSY-11 detection setup. Only detectors used for the measurements of the proton-deuteron elastic scattering and proton-proton quasi-free scattering are shown. Figure taken from [27].

Two body kinematics [37] puts restrictions for angles θ_1 and θ_2 of both scattered particles:

$$\tan\theta_2 = \tan\theta_1 \cdot f(\theta_1^*), \tag{4.4}$$

where

$$f(\theta_1^*) = \left(\frac{\cos\theta_1^* + \frac{s+m_p^2-m_d^2}{s-m_p^2+m_d^2}}{1-\cos\theta_1^*}\right) \tag{4.5}$$

is a function of the scattering angle of the proton in the proton-deuteron center of mass frame and s, m_p, m_d denote the square of the total energy in the CM system, proton mass and deuteron mass respectively. Taking relation 4.4 into account one expects for the proton-deuteron elastic scattering a correlation between the position of one of these particles in the position sensitive silicon detector (denoted as Si_{mon} in fig. 4.1) and the position of the second particle in S1 scintillator. Monte-Carlo results for the proton-deuteron elastic scattering are shown in fig. 4.2.

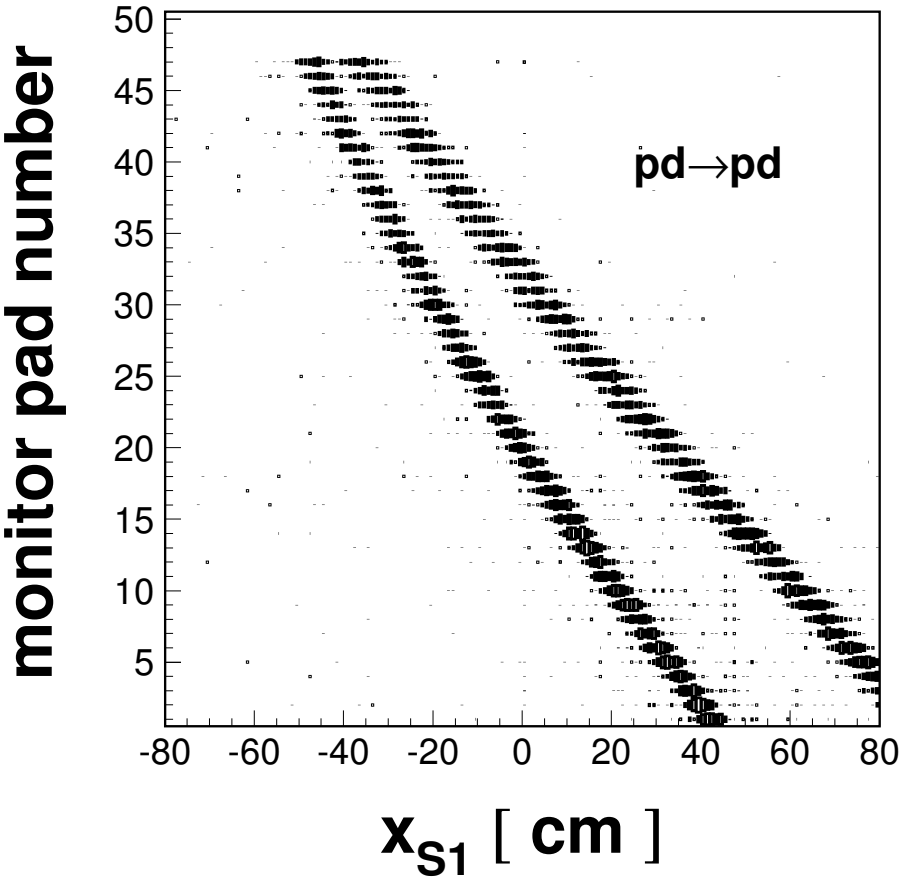

Figure 4.2: Proton-deuteron elastic scattering - correlation between the position of one scattered particle in the S1 detector and the position of the second particle in the silicon detector Si$_{mon}$ at a beam momentum at $P_{beam} = 3350\ MeV/c$.

The events form two correlation curves, which at the shown range are close to straight lines. For the upper line the proton is registered in the S1 and the deuteron in silicon detector, and the lower line shows the case when the deuteron reaches S1 and the proton hits Si$_{mon}$. In the simulations the geometrical spread of the beam and target as well as the resolution of the position determination in the S1 detector and the granuality of the silicon monitor have been taken into account. One can see that the resolution is good enough to distinguish between the two cases.

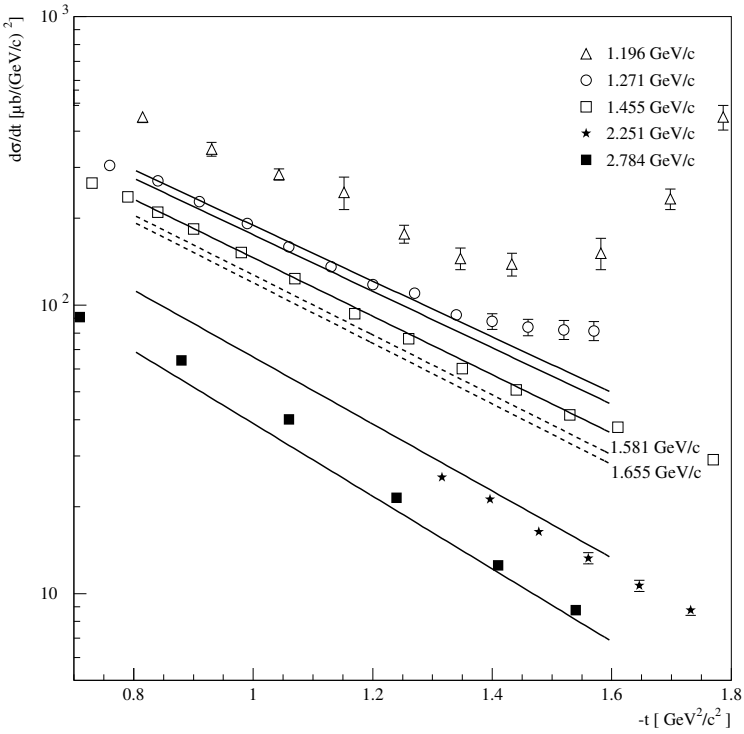

Figure 4.3: Preliminary parametrization of pd-elastic data from literature. Figure taken from [38]. The momentum transfer is given by $t = 2\ k^2\ (\cos\theta^* - 1)$, where k is the momentum of one particle before the reaction in the center-of-mass (CM) frame and θ^* is the scattering angle in the CM system.

Total and differential cross sections for pd-elastic scattering shown in fig. 4.3 are well known from the literature and have been parametrized [38] in the momentum range corresponding to threshold production of η and η' mesons. $\frac{\Delta N}{\Delta\Omega^*}$ is determined from the experiment. This allows to calculate the luminosity L using eq. 4.3.

4.2 Proton-proton quasi-free scattering

Apart from the case when the proton is elastically scattered on a deuteron, reactions of quasi-free proton-proton scattering will also occur. In this kind of reactions a beam proton collides with the proton bound inside a deuteron, which can result in the deuteron break up. Both protons can be afterwards detected in coincidence by the silicon detector and the S1 scintillator. In this case, due to the equal

masses of the scattered particles, equation 4.4 reduces to:

$$\tan\theta_1 \cdot \tan\theta_2 = \frac{1}{\gamma_{cm}^2}. \tag{4.6}$$

Monte-Carlo calculations for this case have been performed and are shown in figure 4.4.

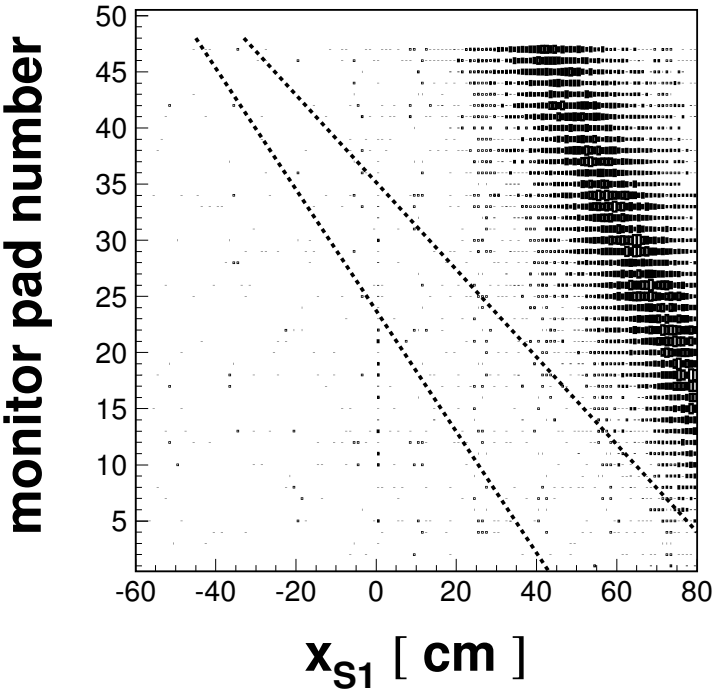

Figure 4.4: Quasi-free proton-proton scattering for the $pd \rightarrow p_{sp}pn$ reaction at $P_{beam} = 3350$ MeV/c (compare fig. 4.2).

Dotted lines shown in this figure represent the correlation for the pd-elastic scattering as depicted in fig. 4.2. Similarly to pd-elastic scattering the correlation between hits in silicon pads and S1 modules is close to the straight line. However, in this case the events are much larger smeared due to the Fermi motion of the proton bound inside the deuteron. If target protons were at rest for each collision, the smearing would be similar to that of fig. 4.2.

As a conclusion let us point out the nice feature that pp quasi-free scattering can be easily distinguished from pd-elastic events in the Si_{mon}—S1 coincidence graph. Thus, it will be possible to determine the luminosity by the measurement of the two reactions shortly presented in this Chapter.

5. Simulation results

Due to the Fermi motion of nucleons bound inside the deuteron and as a consequence of the excess energy variation, described in section 2.3, the proton beam momentum has to be determined in order to find out the optimum conditions for the $pn \to pn\eta(\eta')$ reactions. Monte-Carlo calculations were performed by means of a dedicated programme which is described in details in Appendix C.

5.1 Determination of the excess energy resolution

Since the total cross section for the production of η and η' close to threshold varies drastically with excess energy Q (see for instance fig. 2.1), the latter has to be precisely specified for each event.

Besides the "pure" excess energy Q generated in the Monte-Carlo, which distributions for the $pn \to pn\eta$ and $pn \to pn\eta'$ reactions are shown in fig. 2.3, the simulation programme calculates also the excess energy as it would be measured in the experiment, taking into account the angle and energy resolutions of the spectator detector, the finite geometrical beam and target overlap as well as the smearing of the beam momentum. Linking equations 2.2 and 2.3 together, this "experimental" value of the excess energy can be written as:

$$Q_{exp} = \sqrt{[(P_p + \Delta P_p) + (P_n + \Delta P_n)]^2} - \sum_i m_i, \tag{5.1}$$

where the notation from Chapter 2 has been kept and the four-vectors ΔP_p and ΔP_n represent the experimental smearing of the proton and neutron four-momentum assumed in the calculations[1].

The difference between the Q generated and the Q_{exp} value:

$$\Delta Q = Q - Q_{exp} \tag{5.2}$$

has been calculated for each event and its distribution for the $pn \to pn\eta(\eta')$ reactions is presented in figures 5.1.a and 5.1.b, for the beam momenta of 2070 **MeV/c and** 3340 **MeV/c, respectively.**

[1] For more details see Appendix C.

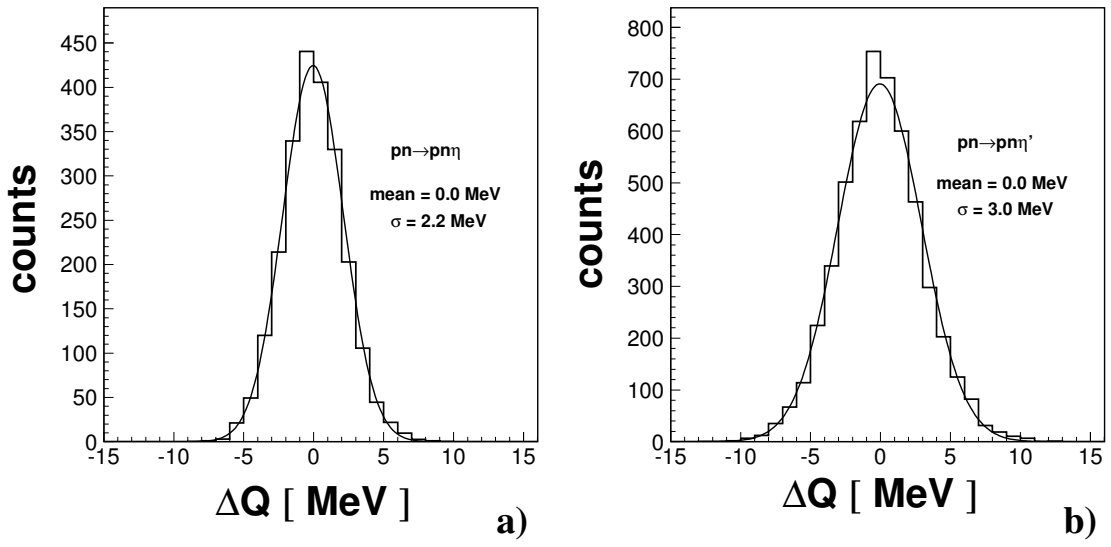

Figure 5.1: Difference between Q generated and Q reconstructed for the reactions (a) $pn \to pn\eta$**; (b)** $pn \to pn\eta'$**. Spectator detector position: (a)** $z_{SD} = -2.6$ **cm, (b)** $z_{SD} = -2.8$ **cm. The neutron detector in both cases was placed at a distance of** 730 **cm from the target in the** 5×5 **configuration.**

For the figures presented above a Gaussian distribution has been fitted and it was found that in the case of the $pn \to pn\eta$ **reaction the inaccuracy in determining the** Q **value is** $\sigma(Q) = 2.2$ **MeV, whereas in the case of** η' **production** $\sigma(Q) = 3.0$ **MeV.**

5.2 Expected rate and beam momentum optimization

For the estimation of the optimum beam momentum only one position of the spectator detector was investigated. For the $pn \to pn\eta$ **reaction the spectator detector was placed as shown in fig. 3.5 at a distance of** $z_{SD} = -3.0$ **cm from the target, where** z_{SD} **denotes the distance along the beam axis between the target and the centre of the detector modules as schematically depicted in fig. 3.5. For the** $pn \to pn\eta'$ **reaction this position was** $z_{SD} = -2.2$ **cm. In the case of** η **production the beam momentum was changed from** 1990 **MeV/c up to** 2170 **MeV/c in** 10 **MeV/c steps. For** η' **production the region of beam momentum varied from** 3210 **MeV/c up to** 3440 **MeV/c [2]. The neutron detector was set in both cases at a distance of** 730 **cm from the target as shown in fig 3.11.b.**

[2] Threshold values of the beam momentum for the production of η and η' mesons on a neutron in rest are $p^{thr}_{pn\to pn\eta} = 1980.5$ MeV/c and $p^{thr}_{pn\to pn\eta'} = 3206.2$ MeV/c. Note that neutron inside the deuteron is not at rest.

The number of reactions that can be registered and reconstructed during one day of measurement, which will be further called an expected rate, was used as a criterion for the identification of the optimum beam momentum. In order to calculate this number, the following procedure has been applied:

- **Since the inaccuracy of determination of the Q value is expected to be about ± 2.5 MeV (see section 5.1), the excess energy range has been divided into several 5 MeV subranges.**

- **The division has been cut at $Q = 40$ MeV because above that energy higher partial waves (higher than the S wave) in the outgoing channel start to play an important role [39]. This makes the description of the outgoing system of particles much more complicated, which was not taken into account in the simulation programme. Additionally, together with the excess energy growth the signal-to-noise ratio decreases, and simultaneously the missing mass spectrum widens making the identification of the reaction much harder as it is well known from the $pp \to ppX$ measurements at the COSY-11 facility [40].**

- **For each out of $i = 1,...,8$ excess energy subranges of Q between 0 and 40 MeV, the detection efficiency has been calculated as:**

$$E_{ff}(i) = \frac{N_{Q>0}}{N_{generated}} \cdot \frac{\sum_{accepted(i)} (W_{FSI} \cdot W_{ND})}{\sum_{Q>0} W_{FSI}}, \tag{5.3}$$

where the first factor describes the ratio between the number of events with $Q > 0$ which can lead to the $pn \to pn\eta(\eta')$ reaction and the total number of generated $pd \to pnpX$ collisions. The second factor takes into consideration the acceptance of the COSY-11 detection system, where W_{FSI} and W_{ND} account for the proton-neutron final state interaction and the neutron detection efficiency, respectively. Details of the W_{FSI} and W_{ND} weights calculations are described in Appendix C.

As an example, the detection efficiency as a function of the excess energy (as it was calculated in the simulations) is shown if fig. 5.2.

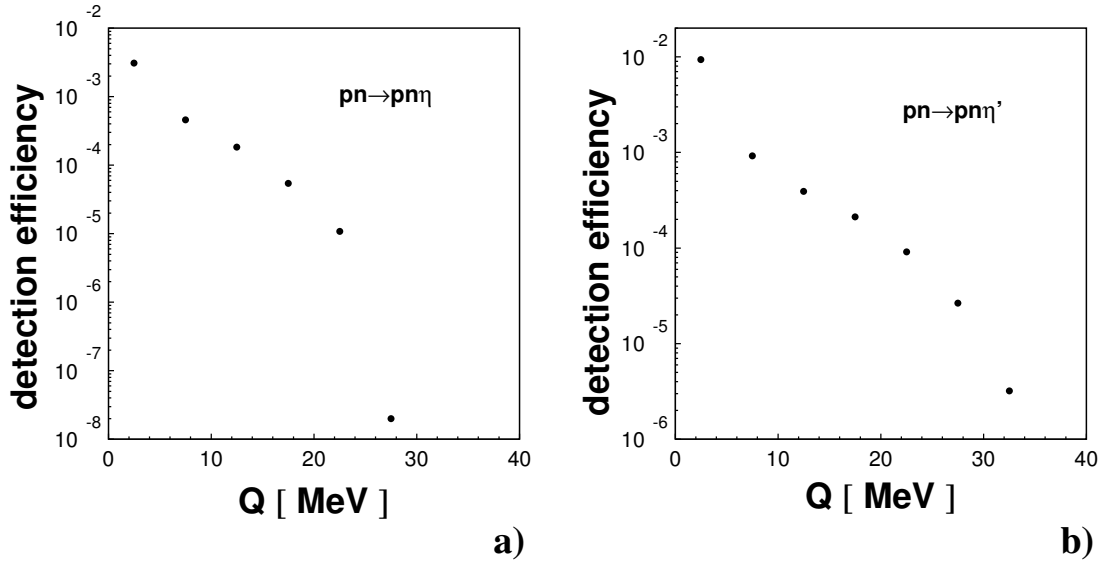

Figure 5.2: Detection efficiency for (a) the $pn \to pn\eta$ reaction at $P_{beam} = 2070$ MeV/c and $z_{SD} = -2.6$ cm, (b) the $pn \to pn\eta'$ reaction at $P_{beam} = 3340$ MeV/c and $z_{SD} = -2.8$ cm. In both cases neutron detector was placed at the distance of 730 cm in the 5×5 configuration. One can clearly seen strong decreasing of the detection efficiency with the excess energy growth.

- **The expected rate of $\eta(\eta')$ meson production corresponding to the i–th excess energy subrange is given by:**

$$N^{\eta(\eta')}(i) = E_{ff}(i) \cdot \sigma(i)^{\eta(\eta')} \cdot L, \tag{5.4}$$

where L stands for the luminosity and it was assumed in the calculations to be equal to a typical conservative value of:

$$L = 2 \cdot 10^{30} \frac{1}{cm^2 s} \approx 172.8 \frac{1}{nb \cdot day}. \tag{5.5}$$

- **The total cross sections ($\sigma(i)$) have been calculated for the centre of each excess energy subrange. For the $pn \to pn\eta$ reaction the parametrization of the cross section described in Appendix C (fig. C.2) had been used, whereas for $pn \to pn\eta'$ two models were considered corresponding to the both extreme cases of η' meson production mentioned in Chapter 1. In the case of the glue excitation model the total cross section was assumed to be the same as for the $pp \to pp\eta'$ reaction and a proper fit to the data measured by the COSY-11 collaboration [41] have been performed. For the meson exchange model the expected ratio $R_{\eta'}$ is assumed to be equal to 6.5, thus in this case the same parametrization has been used, but all cross section weights were multiplied by the factor 6.5.**

Linking two latest points together one can calculate the expected rate for each excess energy subrange as illustrated in fig. 5.3.

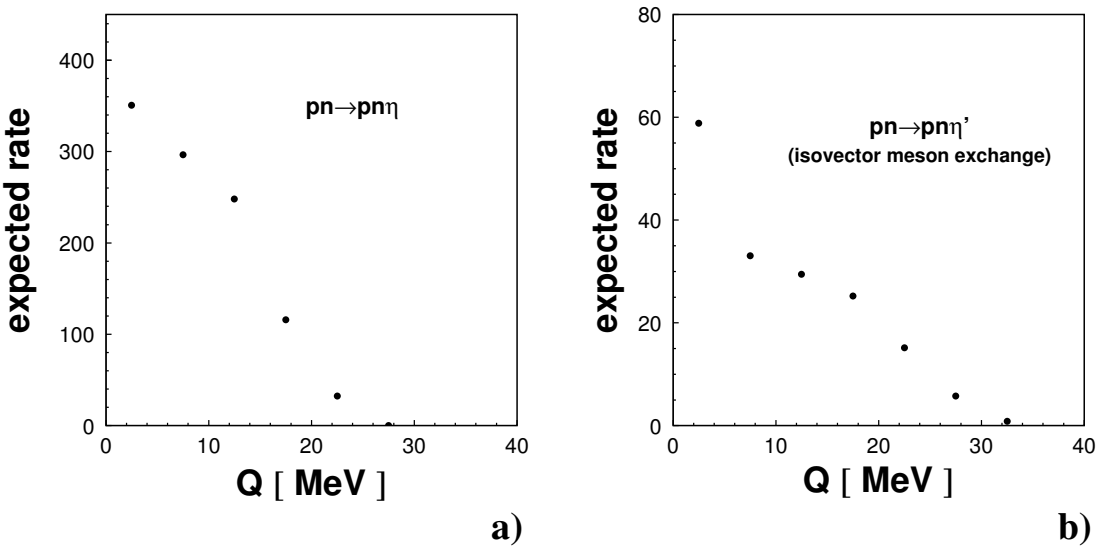

Figure 5.3: Expected number of (a) $pn \to pn\eta$ reactions and (b) $pn \to pn\eta'$ reactions (per day and per 5 MeV bin) as a function of the excess energy Q. Calculations were performed under the same assumptions as in fig. 5.2. For the $pn \to pn\eta'$ reaction the isovector meson exchange model was taken into account.

- **Total expected rate for $\eta(\eta')$ meson production is equal to the sum of the rates over all Q subranges:**

$$N^{\eta(\eta')} = \sum_{i=1}^{8} N^{\eta(\eta')}(i), \tag{5.6}$$

and is shown in fig. 5.4 as a function of a beam momentum.

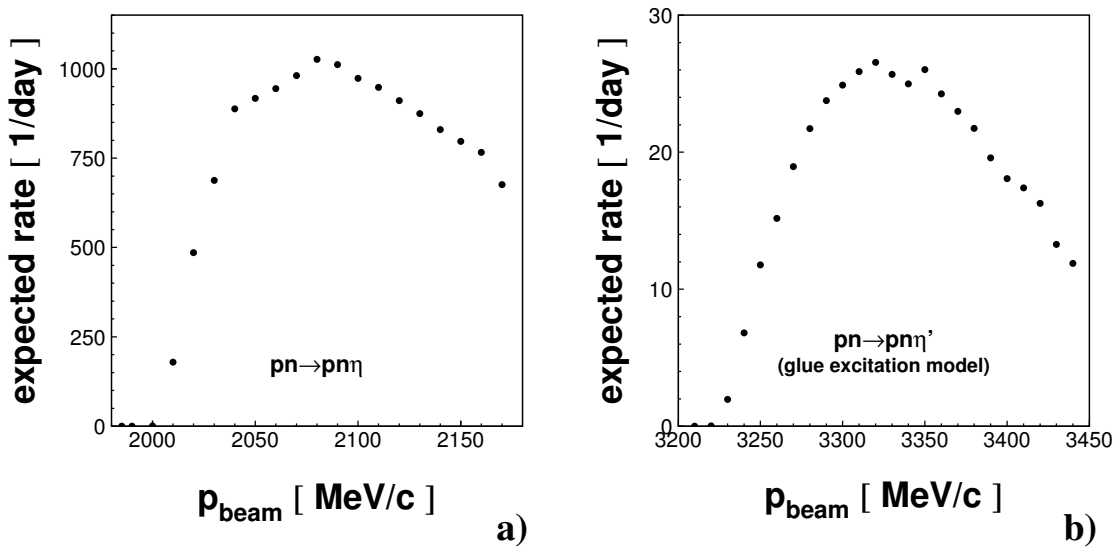

Figure 5.4: (a) Expected number of $pn \to pn\eta$ reactions registered per day as a function of a beam momentum. The neutron detector was placed at a distance of 730 cm, whereas the spectator detector position was set to be $z_{SD} = -3.0$ cm. (b) The same plot for the $pn \to pn\eta'$ reaction. In this case the spectator detector was placed at $z_{SD} = -2.2$ cm. In the calculations for the $pn \to pn\eta'$ reaction the glue excitation model was taken into account.

It is worth to mention that from the above figures the optimum beam momentum can be determined only in the first order, since the graphs do not show the behaviour of the expected rate as a function of the spectator detector position. Therefore further calculations were required in order to infer the optimum beam momentum with higher precision as well as with the optimum position of the spectator detector.

5.3 Position optimization of the spectator detector

In order to carry out the task put at the end of the previous section, the beam momentum range from 2050 MeV/c to 2100 MeV/c for the $pn \to pn\eta$ reaction was examined, whereas for the $pn \to pn\eta'$ reaction the calculations were performed for the beam momentum range between 3310 MeV/c and 3360 MeV/c. In both cases the beam momentum has been changed in 10 MeV/c steps. For the fixed value of the beam momentum, the Monte-Carlo calculations have been performed varying the distance z_{SD} along the beam axis between the target and the spectator counter in 2 mm steps. The technical needs for the installation of the spectator detector make impossible measurements for distances $|z_{SD}| < 1.6$ cm. This is due to the overlapping of the beam flux with the frame that holds the spectator detector modules.

The detection efficiencies calculated from equation 5.3 for the $pn \to pn\eta(\eta')$ reactions as a function of the beam momentum and the spectator detector position along the beam axis are depicted in fig. 5.5.

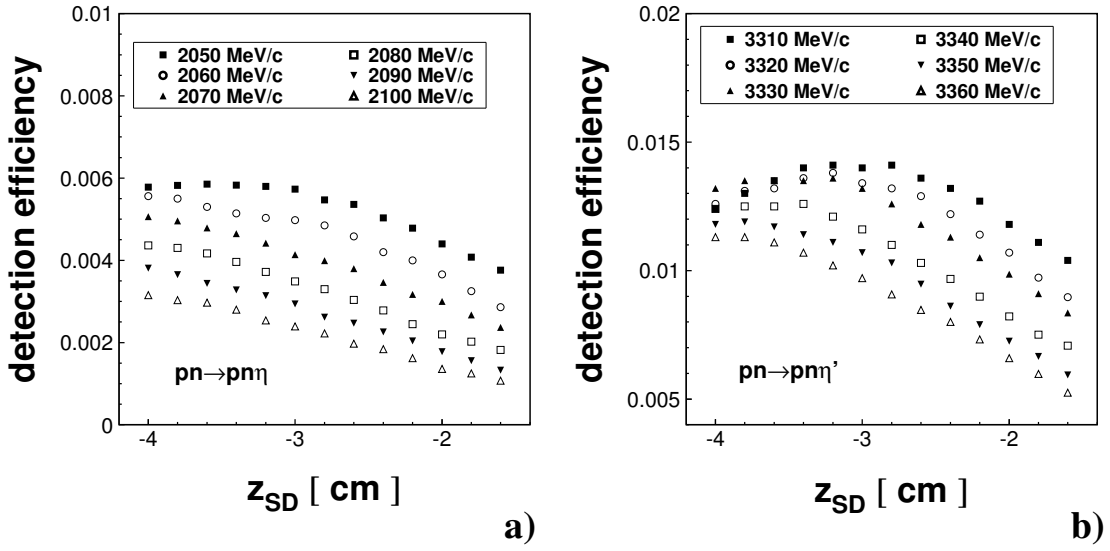

Figure 5.5: Detection efficiency as a function of beam momentum and spectator detector position for the $pn \to pn\eta$ (a) and $pn \to pn\eta'$ reactions (b).

The detection efficiency decreases with growing beam momentum and the maxima of the curves shown in fig. 5.5 move toward higher distances z_{SD} when increasing the beam momentum. The geometrical acceptance of the spectator detector would reach its maximum at $z_{SD} = 0$ cm. However at that point the acceptance of the other components of the COSY-11 detection system decreases due to the large perpendicular component of the target neutron momentum. Thus, the observed structure in fig. 5.5 results from these two effects.

As it is pointed out in Appendix C, the detection efficiency is not the only sufficient indication of the optimum position for the spectator detector, but one has to calculate its convolution with the cross section and to normalize it in order to obtain the expected rate of the events per one day of measurements as it was described in section 5.2. Such calculations have been performed and figures 5.6 and 5.7 show the results for the $pn \to pn\eta$ and $pn \to pn\eta'$ reactions, respectively.

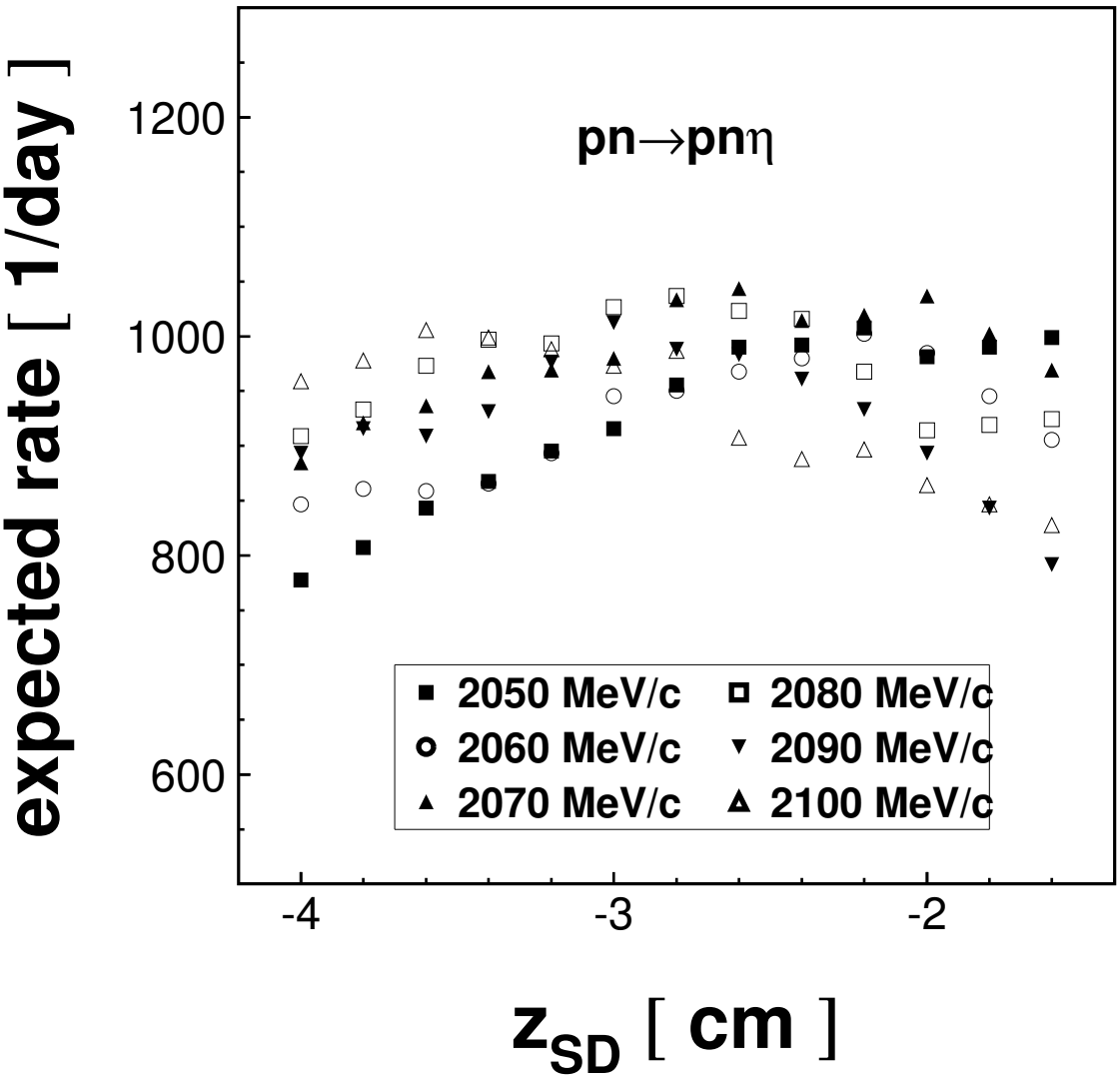

Figure 5.6: Expected rate of $pn \to pn\eta$ reactions. In the calculations the total cross section was parametrized according to equation C.10. The neutron detector was placed at a distance 730 cm from the target.

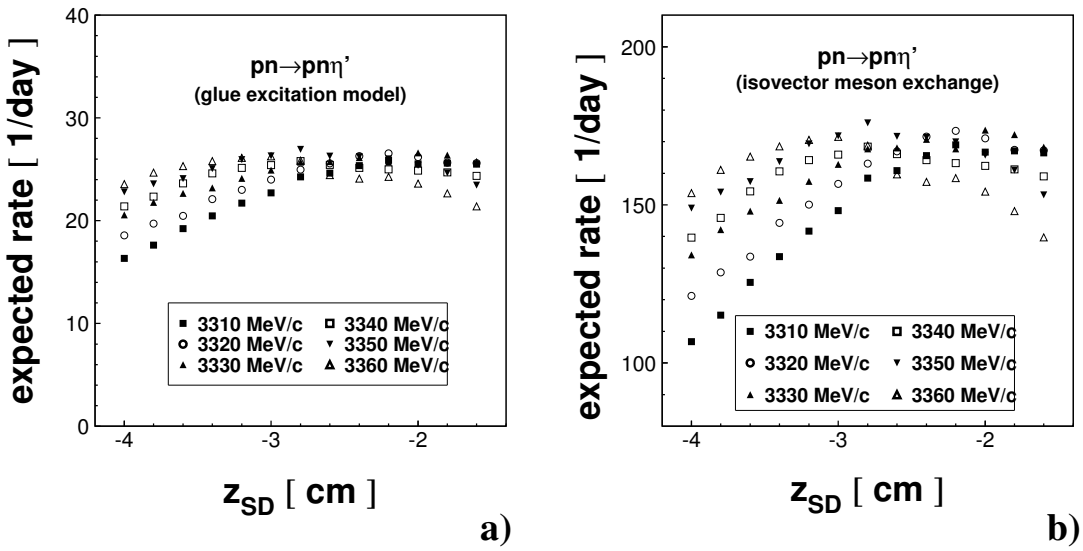

Figure 5.7: (a) Expected number of $pn \to pn\eta'$ reactions per day as a function of the beam momentum and spectator detector position along the beam axis. The neutron detector was placed at a distance of 730 cm from the interaction point. In the calculations the total cross section for the $pn \to pn\eta'$ reaction was taken to be equal to the cross section for the $pp \to pp\eta'$ reaction (glue excitation model). (b) Same plot as before for the cross section dependence as it would be in the isovector meson exchange model. Here, the total cross section for the $pn \to pn\eta'$ reaction was assumed to be 6.5 times larger than in the case of glue excitation model.

In the calculations of the expected rate a conservative value of the luminosity (equation 5.5) has been assumed. In both cases, i.e. for the production of η and η', the expected rates show a similar behaviour when varying the beam momentum and z_{SD}. For the beam momentum close to the threshold exhibit a rather sharp slope whereas increasing the beam energy causes that they become more flat, which is a desired feature, since any inaccuracy in determining the spectator detector position will lead to small errors.

In the case of the $pn \to pn\eta$ reaction the candidates for the optimum beam momentum are the curves for 2070 MeV/c and 2080 MeV/c and in the case of the $pn \to pn\eta'$ reaction the ones for 3340 MeV/c and for 3350 MeV/c, at which value of the beam momentum we have a maximum in the number of registered reactions.

Another, very important criterion in finding the optimum experimental conditions for the considered reactions is the width of the missing mass spectrum, which is also a function of the beam momentum and spectator detector position. The behaviour of the width of the missing mass spectrum (FWHM) for both reactions is shown in tables 5.1 and 5.2.

Summarising, taking into account all features presented above, i.e.

p_{beam} $[MeV/c]$	z_{SD} $[cm]$	FWHM of missing mass spectrum $[MeV] \pm 0.5\ MeV$
2070.	-1.6	5.
	-1.8	5.
	-2.0	5.
	-2.2	6.
	-2.4	6.
	-2.6	6.
	-2.8	6.
	-3.0	5.
	-3.2	5.
	-3.4	4.
	-3.6	4.
	-3.8	4.
	-4.0	4.
2080.	-1.6	7.
	-1.8	7.
	-2.0	7.
	-2.2	5.
	-2.4	6.
	-2.6	5.
	-2.8	6.
	-3.0	6.
	-3.2	5.
	-3.4	5.
	-3.6	5.
	-3.8	5.
	-4.0	4.

Table 5.1: Missing mass spectrum width for the $pn \to pn\eta$ reaction as a function of the beam momentum and spectator detector position.

p_{beam} $[MeV/c]$	z_{SD} $[cm]$	FWHM of missing mass spectrum $[MeV] \pm 0.5\ MeV$
3340.	-1.6	9.
	-1.8	9.
	-2.0	9.
	-2.2	8.
	-2.4	9.
	-2.6	8.
	-2.8	7.
	-3.0	7.
	-3.2	7.
	-3.4	7.
	-3.6	7.
	-3.8	7.
	-4.0	6.
3350.	-1.6	10.
	-1.8	10.
	-2.0	9.
	-2.2	9.
	-2.4	9.
	-2.6	9.
	-2.8	8.
	-3.0	7.
	-3.2	7.
	-3.4	7.
	-3.6	7.
	-3.8	7.
	-4.0	7.
3360.	-1.6	11.
	-1.8	10.
	-2.0	10.
	-2.2	9.
	-2.4	9.
	-2.6	8.
	-2.8	9.
	-3.0	8.
	-3.2	8.
	-3.4	8.
	-3.6	8.
	-3.8	7.
	-4.0	7.

Table 5.2: Missing mass spectrum width for the $pn \to pn\eta'$ reaction as a function of the beam momentum and spectator detector position.

- **high expected rate**
- **flat slope of the expected rate curve**
- **good missing mass resolution**

let us conclude that for the $pn \to pn\eta$ reaction the optimum beam momentum is equal to:

$$\mathbf{p_{beam}^{pn\to pn\eta} = 2070 \pm 5\ \frac{MeV}{c}}. \tag{5.7}$$

The best spectator detector position for this case was found to be:

$$\mathbf{z_{SD} = -2.6 \pm 0.1\ cm}. \tag{5.8}$$

For the $pn \to pn\eta'$ reaction the optimum beam momentum is:

$$\mathbf{p_{beam}^{pn\to pn\eta'} = 3340 \pm 5\ \frac{MeV}{c}} \tag{5.9}$$

and the best z_{SD} in this case equal:

$$\mathbf{z_{SD} = -2.8 \pm 0.1\ cm}. \tag{5.10}$$

We expect in the optimum conditions for the $pn \to pn\eta$ reaction the number of measured and reconstructed events per day to be at the order of 1000. The same number for the $pn \to pn\eta'$ reaction is expected to amount to 25 or 170 events per day depending on the dominant production mechanism of the η' meson.

5.4 Arrangement of the neutron detector

In the selection of the best experimental conditions for the $pn \to pn\eta$ and $pn \to pn\eta'$ reactions the most important role play two main quantities, namely the expected rate and the missing mass width. Putting the neutron detector at the higher distance from the target we expect to reduce the missing mass width due to the higher precision of measurements of the neutron four-momentum. On the other hand the expected rate will decrease, because the solid angle covered by the neutron detector is smaller than in the case when the neutron detector is located closer to the target. In order to reduce this effect the configuration of the neutron detector placed farther from the target was designed to be 5×5 (see fig. 3.11.b). This is the compromise between the covering of the solid angle and the neutron detector efficiency which is a function of the path of neutrons inside the detector (which path is on average longer when the detector has more modules put one by one in the direction defined by the beam momentum). The topography of the COSY ring allows to locate the neutron detector in the 5×5 configuration at the

longest distance equal to 730 cm. And this was the position of the neutron detector used in the previous calculations.

Let us check now, what would happen when placing the neutron detector closer to the target. Obviously, we expect to increase the detection efficiency at the cost of loosing the accuracy in determining the neutron four-momentum. This would reflect in the widening of the missing mass spectrum.

Calculations were performed for a neutron detector position at 430 cm from the target. The configuration of the neutron detector was chosen to be 3×8 in order to increase the count rate in the neutron detector with reference to the case when the detector has a 5×5 configuration.

The comparison of the detection efficiency for both locations (and different configurations) of the neutron detector is presented in fig. 5.8.

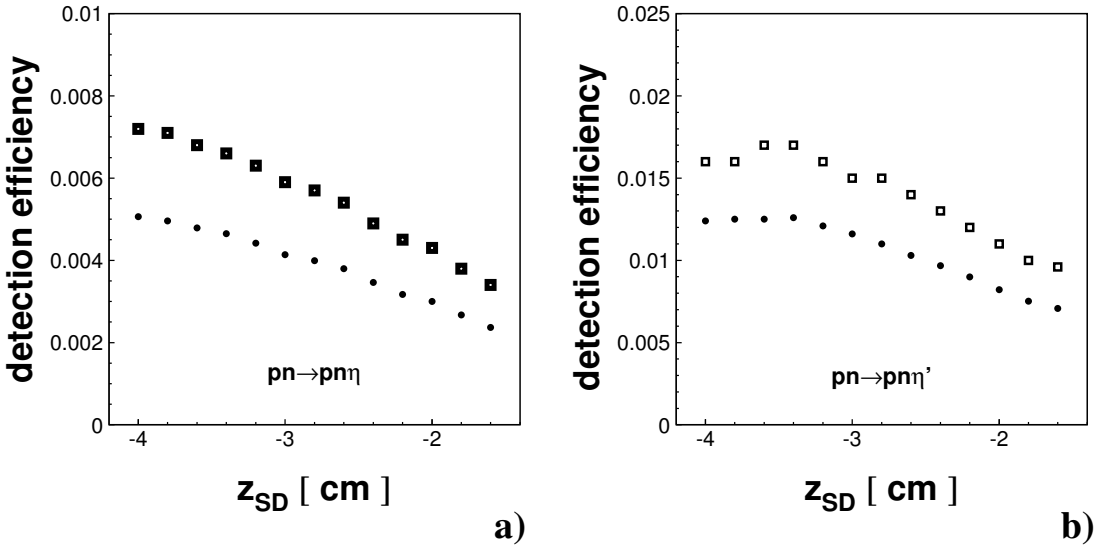

Figure 5.8: (a) Efficiency of the COSY-11 detection system for the $pn \to pn\eta$ reaction at a beam momentum of 2070 MeV/c. (b) The same plot for the $pn \to pn\eta'$ reaction. The beam momentum was set to be 3340 MeV/c. In both figures squares represent the case when the neutron detector was located at 430 cm from the beam in a 3×8 configuration. Circles show the results of simulations in which the neutron detector was put at a distance of 730 cm away from the target in a 5×5 configuration.

For the case when the spectator detector was placed in its optimum position and for the optimum beam momentum (which both have been found in section 5.3), the efficiency of the detection system is higher for the case when the neutron detector is located at 430 cm from the target in a 3×8 configuration rather than in the case when it is placed at 730 cm in a 5×5 configuration. The detection efficiency is higher by about 42% in the case of the $pn \to pn\eta$ reaction and over 35% in the case of the $pn \to pn\eta'$ reaction. With respect to the expected rates, these numbers are 40% and 34%, respectively (see fig. 5.9).

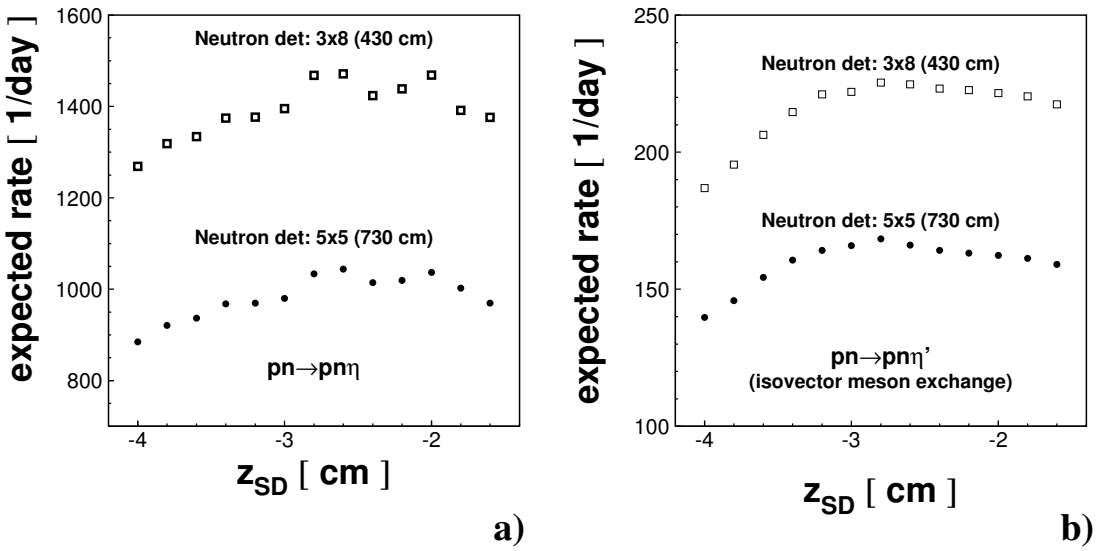

Figure 5.9: **(a) Expected rate of the $pn \to pn\eta$ reaction at a beam momentum of 2070 MeV/c for two different positions and configurations of the neutron detector. (b) The same plot for the $pn \to pn\eta'$ reaction. The beam momentum was set to be 3340 MeV/c. Meaning of the symbols is the same as in figure 5.8.**

As one can see from the above figures, the behaviour of the detection efficiency and of the expected rate is similar in both configurations of the neutron detector. Curves of the expected rate reach their maximum values independently from the configuration of the neutron detector for the same position of the spectator detector as it was found in section 5.3.

What happens to the missing mass peak width when locating the neutron detector closer to the target? Table 5.3 contains the comparison of the missing mass widths for both configurations of the spectator detector and for both considered reactions.

For the $pn \to pn\eta$ reaction differences in the missing mass width, originating from the different configuration of the neutron detector, are small, however they exist. Differences are clearly seen in the case of the $pn \to pn\eta'$ reaction where the missing mass peak width in the case of a 3×8 configuration of the neutron detector is on average 2 MeV wider than it would be for a 5×5 configuration. Since it would be desirable to have the best missing mass resolution that can be obtained in the $pn \to pn\eta'$ measurements, the experiment will be performed with the 5×5 configuration of the neutron detector, located at the distance of 730 cm from the target. At least in the first runs of the experiment we would like to go in the direction of the more precise measurements of the neutron four-momentum, aiming in the better signal-to-background ratio in the missing mass spectrum, even at the cost of loosing almost 35% of the events. Additionally at that position we expect lower background from the neutrons scattered or produced at the COSY-11 vacuum chamber.

z_{SD} $[cm]$	FWHM of missing mass spectrum $[MeV] \pm 0.5\ MeV$ $pn \to pn\eta$ 5×5	FWHM of missing mass spectrum $[MeV] \pm 0.5\ MeV$ $pn \to pn\eta$ 3×8	FWHM of missing mass spectrum $[MeV] \pm 0.5\ MeV$ $pn \to pn\eta'$ 5×5	FWHM of missing mass spectrum $[MeV] \pm 0.5\ MeV$ $pn \to pn\eta'$ 3×8
-1.6	5.	7.	9.	11.
-1.8	5.	6.	9.	10.
-2.0	5.	6.	9.	10.
-2.2	6.	6.	8.	10.
-2.4	6.	6.	9.	10.
-2.6	6.	6.	8.	10.
-2.8	6.	7.	7.	9.
-3.0	5.	6.	7.	9.
-3.2	5.	6.	7.	9.
-3.4	4.	6.	7.	8.
-3.6	4.	6.	7.	9.
-3.8	4.	5.	7.	9.
-4.0	4.	5.	6.	8.

Table 5.3: Comparison of the missing mass peak width for the $pn \to pn\eta(\eta')$ reactions for both configurations of the neutron detector. Calculations were performed with the proton beam momenta of 2070 MeV/c and 3340 MeV/c depending on the produced meson.

6. Summary and perspectives

Until today there have been no data published concerning the η' production in quasi-free proton-neutron collisions. Preparations for an experiment concerning this problem have been described in this thesis. For both considered reactions optimum experimental conditions have been determined. The optimum beam momentum for the $pn \to pn\eta$ quasi-free measurements was found to be $p_{beam}^{pn\to pn\eta} = 2070 \pm 5\,\mathrm{MeV/c}$, whereas for a $pn \to pn\eta'$ reaction this value is $p_{beam}^{pn\to pn\eta'} = 3340 \pm 5\,\mathrm{MeV/c}$. For the first reaction, the optimum position of the spectator detector was predicted to be $z_{SD} = -2.6 \pm 0.1$ cm. In the latter case this position is expected to be $z_{SD} = -2.8 \pm 0.1$ cm. For both reactions placing the neutron detector at a distance of 730 cm from the target in a 5×5 configuration will lead to the relatively small missing mass widths. In the case of η production this width is expected to be 6.0 ± 0.5 MeV, whereas in the case of η' a value of 7.0 ± 0.5 MeV is expected. The spectra of the missing mass for both cases are presented in fig. 6.1.

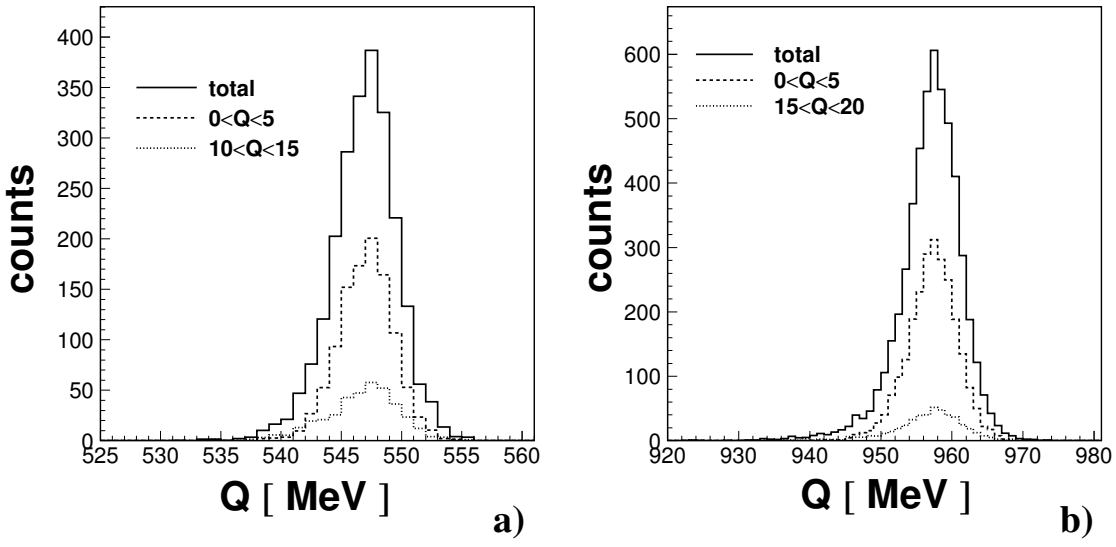

Figure 6.1: Missing mass as reconstructed from Monte-Carlo calculations at the optimum experimental conditions (a) for the $pn \to pn\eta$ reaction and (b) for the $pn \to pn\eta'$ reaction.

The inaccuracy in determining the Q value in the experiment is expected to be $\pm$ 2.2 MeV in the case of the $pn \to pn\eta$ reaction and $\pm$ 3.0 MeV in the case of η' production.

The expected production rate of η mesons is in the order of 1000 events per day, whereas considering two extreme scenarios of η' production, the number of produced η' mesons is expected to be 25 per day, providing that the *glue excitation* model is correct or it would be about 170 in case when the *isovector meson exchange* is the mechanism that describes the η' production close to the threshold. This values have been calculated assuming a luminosity of $L = 2 \cdot 10^{30} \frac{1}{cm^2 s}$.

As it was presented in Chapter 4.1, the luminosity can be determined by simultaneous measurement of the elastic $pd \to pd$ scattering. Moreover, it was shown that the quasi-free $pp \to pp$ scattering does not disturb the measurement of $pd \to pd$ elastic scattering — data from these two measurements can be clearly distinguished as depicted in fig. 4.4.

There also exist plans for carrying out the investigations of the close to threshold meson production in neutron-neutron collisions (fig. 6.2).

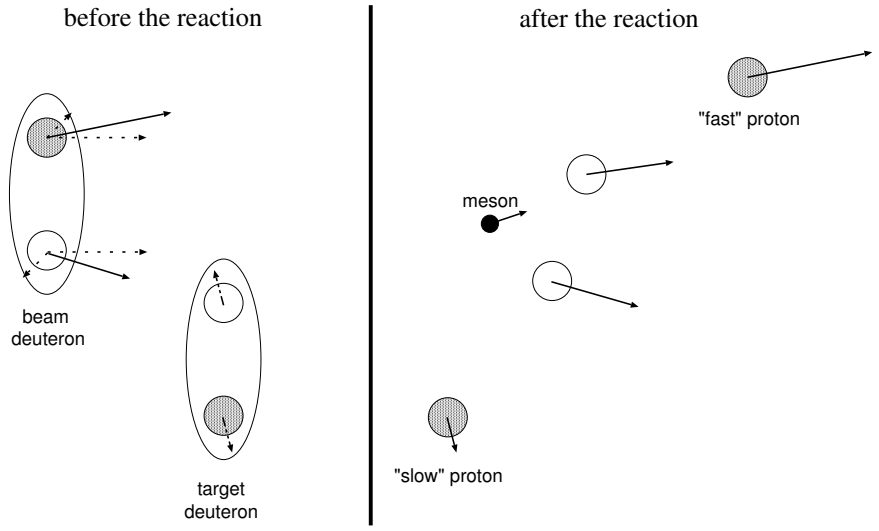

Figure 6.2: Schematic picture of the double quasi-free $nn \to nnX^0$ reaction. Short dotted arrows represent the Fermi momenta of nucleons inside the deuteron. Protons are depicted as shaded circles, whereas neutrons are represented by the open circles.

The measurements would be based on the double quasi-free collision of neutrons bound inside the deuterons. There would be two spectator protons: a fast one, originating from the beam deuteron and a slow one, coming from the target deuteron. The registration of both these spectators would allow to determine the excess energy. The slow spectator may be registered by the spectator detector described in this thesis (section 3.5), whereas fast spectators can be detected by the magnetic spectrometer, utilizing the same method as for the fast beam proton in case of the $pd \to pnp_{sp}X$ reaction. The $nn \to nnX$ reaction can be identified by the

additional registration of both outgoing neutrons.

These pioneering experiments have been proposed in August 2001 [39]. They would allow for instance:

- **to study the charge symmetry breaking by comparing the cross sections for the $pp \to pp\eta$ and $nn \to nn\eta$ reactions,**
- **to infer the neutron-neutron and neutron-Meson scattering lengths,**
- **complementary studies on the production of K^+K^- pairs [39].**

At present, the available deuteron beam energies at the COSY synchrotron allow for π and η meson production in $nn \to nnX^0$ reactions. However, in order to produce heavier mesons in neutron-neutron collisions deuteron beam momenta of about 7 GeV/c are required [39].

7. Acknowledgments

I am very grateful to all the people who served me with their help during bringing to life this thesis. I am really sorry that with my poor english I cannot express how much grateful I am. I would like to especially thank to:

- **dr. Paweł Moskal for introducing me to the wonderful world of meson physics, for suggesting a very interesting project and guiding me through it, for his trust and valuable time shared with me, for plenty of interesting ideas used in this work and for the enormous patience in correcting this thesis. It is a pure pleasure to work with you, Paweł!**
- **Prof. Bogusław Kamys for the trust put on me, lots of discussions and ideas concerning my work and lots of patience in reading and correcting this thesis;**
- **Prof. Kurt Kilian, Prof. Walter Oelert and dr. Dieter Grzonka for their great hospitality and for inviting me to visit the Research Centre Jülich;**
- **Prof. Walter Oelert for giving me possibility to work with the COSY-11 group;**
- **Prof. Lucjan Jarczyk for the interesting lectures on the meson physics and a lot of help with my seminars and sugestions concerning this thesis;**
- **Prof. Reinhard Kulessa for allowing me preparing this thesis in the Nuclear Physics Department of the Jagellonian University;**
- **dr. Magnus Wolke for correcting this thesis and for plenty time spent on explaining me the basics of DAQ;**
- **all the COSY-11 members for their help and friendly atmosphere during the beamtimes and meetings;**
- **dr. Paweł Kulessa and Roman Skibiński for reading parts of this thesis and for their useful comments;**
- **my dear colleagues Aleksandra Białek, Anna Kowalczyk, Aleksandra Wrońska, Paweł Brylski, Tomasz Bryś, Piotr Hawranek, dr. Wojciech Klimala, Borys Piskor-Ignatowicz, Jacek Pulut and Mariusz Wojciechowski for the great atmosphere of daily work;**

- **Arkadiusz Bubak, Thomas Götz, Christian Kolf, Tomasz Rożek and Peter Winter for roof over my head, when I needed it during my stays in Jülich;**
- **Żaneta and Paweł Moskal for the hospitality and delicious suppers and cakes;**
- **my Parents and the rest of the Family for the love and permanent support during the 5 years of my studies;**
- **and finally to my beloved Beata Tomasik for her great love and support, understanding and enormous patience...**

A. η' mass problem

According to QCD, mesons are bound states of quark-antiquark systems $(q\bar{q})$. From the three lightest quarks, namely u, d and s quarks, nine possible $q\bar{q}$ combinations can be built. This set of SU(3) mesons includes an octet and a singlet:

$$\mathbf{3} \otimes \bar{\mathbf{3}} = \mathbf{8} \oplus \mathbf{1}. \tag{A.1}$$

The ground state pseudoscalar meson nonet is depicted in fig. A.1.

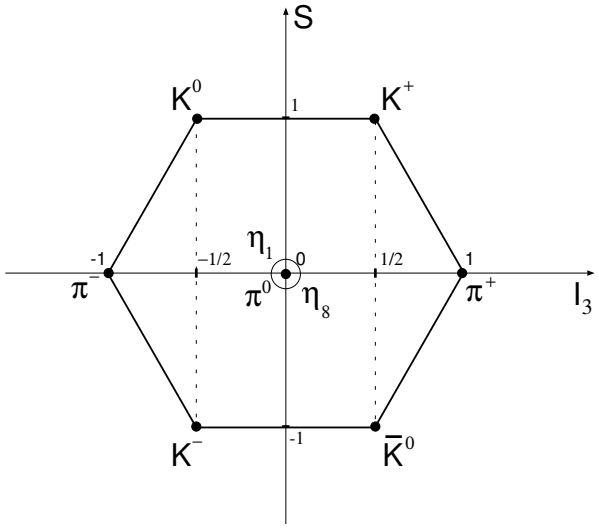

Figure A.1: Ground state pseudoscalar meson nonet.

The singlet SU(3) state — η_1 — corresponds to the following combination of quarks:

$$\eta_1 = \frac{1}{\sqrt{3}}(u\bar{u} + d\bar{d} + s\bar{s}). \tag{A.2}$$

Both η_1 and η_8, the latter belonging to the SU(3) octet:

$$\eta_8 = \frac{1}{\sqrt{6}}(u\bar{u} + d\bar{d} - 2s\bar{s}), \tag{A.3}$$

are not real physical states. Real mesons — η and η' — are mixtures of these pure SU(3) states:

$$\begin{aligned} \eta &= cos(\theta) \cdot \eta_8 - sin(\theta) \cdot \eta_1, \\ \eta' &= sin(\theta) \cdot \eta_8 + cos(\theta) \cdot \eta_1, \end{aligned} \tag{A.4}$$

Meson	Calculated mass [MeV/c^2]	Observed mass [MeV/c^2]
π	140	138
K	484	496
η	559	549
η'	**349**	**958**
ρ	780	776
ω	780	783
K*	896	892
ϕ	1032	1020

Table A.1: Pseudoscalar and vector meson masses. In the calculations the mixing between SU(3) states was neglected. Table taken from [27].

where a pseudoscalar mixing angle $\theta = -15.5^\circ \pm 1.3^\circ$ has been introduced [42]. Putting this value of mixing angle together with linear combinations A.2 and A.3 into eq. A.4 we obtain:

$$\eta = 0.77 \cdot \frac{1}{\sqrt{2}}(u\bar{u} + d\bar{d}) - 0.63 \cdot s\bar{s},$$

$$\eta' = 0.63 \cdot \frac{1}{\sqrt{2}}(u\bar{u} + d\bar{d}) - 0.77 \cdot s\bar{s}. \tag{A.5}$$

Similar amounts of strange and nonstrange quarkonium in η and η' meson should therefore lead to similar masses of these mesons. Masses of the $q\bar{q}$ systems are described by the following equation [27]:

$$m_{q_1\bar{q}_2} = m_{q_1} + m_{\bar{q}_2} + A \cdot \frac{\vec{S}_1 \cdot \vec{S}_2}{m_{q_1} \cdot m_{\bar{q}_2}}, \tag{A.6}$$

where m_{q_i} are constituent masses of the quarks, A is a constant and $\vec{S}_i$ denotes the quark spin. Masses of selected pseudoscalar and vector mesons calculated with the above formula are listed in a table A.1.

There is an agreement within 2% between calculated and experimental masses for all mesons except the η' meson, for which the calculated mass is almost 3 times smaller than the observed one. According to equation A.6 in the extreme case when the η' meson would be a pure $s\bar{s}$ system, its mass would be equal to 768 MeV/c^2, which is still almost 200 MeV/c^2 less than the observed mass of this meson. The problem of the η' mass underestimation is even more surprising if one takes into account that equation A.6 describes well not only light meson masses but also the masses of other hadrons like tensor mesons or baryons.

How to explain that large observed mass of the η' meson? Two gluon annihilation processes $gg \leftrightarrow q\bar{q}$ might contribute to the SU(3)-flavour singlet state [43, 44].

Due to the small pseudoscalar mixing angle such an additional gluon-induced interaction should mainly affect the properties of the η' which is principally built out of the SU(3)-flavour singlet state. In order to reproduce the observed η' mass, a gluonium component ranging between 29% and 53% is required [27, 45]. According to [1] gluonic degrees of freedom generate about $300-400$ MeV/c of both η and η' mesons.

Other possible states predicted by the QCD theory that may have a contribution to the η' wave function are for example hybrids containing glue-like $q\bar{q}g$ states, radially excited $q\bar{q}$ states or heavier quarkonia like charmonium, i.e. $c\bar{c}$ states (for a more details see [27] and references therein). Out of these possibilities the most significant one is the gluonium admixture.

B. Deuteron wave function — CD-Bonn and Paris potentials

The analytical representation of the deuteron wave function in a configuration space can be written as [19]:

$$u_a(r) = \sum_{j=1}^{n} C_j \exp(-m_j r) \tag{B.1}$$

$$w_a(r) = \sum_{j=1}^{n} D_j \exp(-m_j r)(1 + \frac{3}{m_j r} + \frac{3}{m_j^2 r^2}) \tag{B.2}$$

where $u_a(r)$ is the representation of the deuteron S–wave, $w_a(r)$ represents its D–wave component. These functions depend on the relative distance r between the nucleons bound inside the deuteron. C_j and D_j are the coefficients to be calculated. The coefficients m_j are given by:

$$m_j = \alpha + (j-1)m_0 \tag{B.3}$$

with $m_0 = 1$ fm^{-1}, $\alpha = \frac{\sqrt{2m_{p-n}|B_d|}}{\hbar} = 0.2315380$ fm^{-1}, where $2 \cdot m_{p-n} = 938.91852$ MeV and $B_d = -2.224575$ MeV are the neutron-proton reduced mass and the deuteron binding energy, respectively.

The momentum distribution of nucleons inside the deuteron can be derived from the deuteron wave functions in momentum space. These can be obtained from the space representation of the deuteron wave function by means of the Fourier transformation. Under this transformation we obtain the following deuteron wave functions in terms of momentum coordinates:

$$\frac{\psi_0^a(p)}{p} = \sqrt{\frac{2}{\pi}} \sum_{j=1}^{n} \frac{C_j}{p^2 + m_j^2}, \tag{B.4}$$

$$\frac{\psi_2^a(p)}{p} = \sqrt{\frac{2}{\pi}} \sum_{j=1}^{n} \frac{D_j}{p^2 + m_j^2}, \tag{B.5}$$

where $\psi_0^a(p)$ and $\psi_2^a(p)$ wave functions correspond to $u_a(r)$ and $w_a(r)$, respectively. The boundary conditions: $u_a(r) \to r$ and $w_a(r) \to r^3$ as $r \to 0$ imply the following restrictions for C_j and D_j [19]:

$$\sum_{j=1}^{n} C_j = 0 \tag{B.6}$$

$$\sum_{j=1}^{n} \frac{D_j}{m_j^2} = 0 \tag{B.7}$$

$$\sum_{j=1}^{n} D_j = 0 \tag{B.8}$$

$$\sum_{j=1}^{n} D_j m_j^2 = 0 \tag{B.9}$$

Tables B.1 and B.2 contain coefficients C_j and D_j for the Paris [19] and the CD-Bonn [20] nucleon-nucleon interaction models, respectively.

j	$C_j(fm^{-\frac{1}{2}})$	$D_j(fm^{-\frac{1}{2}})$
1	$0.88688076 \cdot 10^{0}$	$0.23125193 \cdot 10^{-1}$
2	$-0.34717093 \cdot 10^{0}$	$-0.85604572 \cdot 10^{0}$
3	$-0.30502380 \cdot 10^{1}$	$0.56068193 \cdot 10^{1}$
4	$0.56207766 \cdot 10^{2}$	$-0.69462922 \cdot 10^{2}$
5	$-0.74957334 \cdot 10^{3}$	$0.41631118 \cdot 10^{3}$
6	$0.53365279 \cdot 10^{4}$	$-0.12546621 \cdot 10^{4}$
7	$-0.22706863 \cdot 10^{5}$	$0.12387830 \cdot 10^{4}$
8	$0.60434469 \cdot 10^{5}$	$0.33739172 \cdot 10^{4}$
9	$-0.10292058 \cdot 10^{6}$	$-0.13041151 \cdot 10^{5}$
10	$0.11223357 \cdot 10^{6}$	$0.19512524 \cdot 10^{5}$
11	$-0.75925226 \cdot 10^{5}$	**see eq. B.11**
12	$-0.29059715 \cdot 10^{5}$	**see eq. B.11**
13	**see eq. B.10**	**see eq. B.11**

Table B.1: Coefficients for the parametrized deuteron wave functions according to the Paris model [19] (n=13)

j	$C_j(fm^{-\frac{1}{2}})$	$D_j(fm^{-\frac{1}{2}})$
1	$0,88472985 \cdot 10^0$	$0.22623762 \cdot 10^{-1}$
2	$-0.26408759 \cdot 10^0$	$-0.50471056 \cdot 10^0$
3	$-0.44114404 \cdot 10^{-1}$	$0.56278897 \cdot 10^0$
4	$-0.14397512 \cdot 10^2$	$-16079764 \cdot 10^2$
5	$0.85591256 \cdot 10^2$	$0.11126803 \cdot 10^3$
6	$-0.31876761 \cdot 10^3$	$-0.44667490 \cdot 10^3$
7	$0.70336701 \cdot 10^3$	$0.10985907 \cdot 10^4$
8	$-0.90049586 \cdot 10^3$	$-0.16114995 \cdot 10^4$
9	$0.66145441 \cdot 10^3$	**see eq. B.11**
10	$-0.25958894 \cdot 10^3$	**see eq. B.11**
11	**see eq. B.10**	**see eq. B.11**

Table B.2: Coefficients for the parametrized deuteron wave functions according to the CD–Bonn model [20] (n=11)

In order to satisfy equations B.6 — B.9, the last C_j coefficient and the last three D_j for both Paris and CD-Bonn potentials are to be computed from the following formulae [19]:

$$C_n = -\sum_{j=1}^{n-1} C_j \tag{B.10}$$

$$D_{n-2} = \frac{m_{n-2}^2}{(m_n^2 - m_{n-2}^2)(m_{n-1}^2 - m_{n-2}^2)} \cdot \tag{B.11}$$
$$\cdot[-m_{n-1}^2 m_n^2 \sum_{j=1}^{n-3} \frac{D_j}{m_j^2} + (m_{n-1}^2 + m_n^2) \cdot \sum_{j=1}^{n-3} D_j - \sum_{j-1}^{n-3} D_j m_j^2]$$

and two other relations for D_{n-1} and D_n can be obtained by circular permutation of n-2, n-1 and n. The missing coefficients are equal to:

$$C_{13} = -0.48157368E + 4,$$
$$D_{11} = -0.15634324E + 5,$$
$$D_{12} = 0.66231090E + 4,$$
$$D_{13} = -0.11698185E + 4,$$

for the Paris potential, and

$$C_{11} = 0.42260718E + 2,$$
$$D_9 = 0.13128923E + 4,$$
$$D_{10} = -0.51438076E + 3,$$
$$D_{11} = 0.65803145E + 2.$$

for the CD–Bonn model.

In order to check the accuracy of calculations, summations B.6–B.9 have been done. Table III contains the sums B.6–B.9 for both potential models.

Table B.3: Sums B.6–B.9

equation	Paris model	CD-Bonn Model
B.6	0.0	0.0
B.7	$3.2 \cdot 10^{-13}$	$-7 \cdot 10^{-15}$
B.8	$2.6 \cdot 10^{-11}$	$-8 \cdot 10^{-13}$
B.9	$3.7 \cdot 10^{-9}$	$-9 \cdot 10^{-11}$

As one can see from inspection of table B.3 the accuracy is satisfactory for our considerations.

Coefficients C_j, $D_j(j = 1,13)$ for the Paris parametrization of the deuteron wave function and C_j, $D_j(j = 1,11)$ for the CD-Bonn model together with the formulae B.4 and B.5 give the analytic form of the deuteron S and D wave functions. The normalized nucleon momentum distribution function can be expressed as:

$$f(p) = p^2[(\psi_0^a)^2 + (\psi_2^a)^2]. \tag{B.12}$$

The distributions are presented in fig. 2.2. This function is normalized so that:

$$\int_0^\infty f(p)dp = 1. \tag{B.13}$$

Subprograms `paris.f` **and** `cdbonn.f` **use equation B.12 in order to calculate the momentum distribution of nucleons inside the deuteron. These subprograms are called by the main program described in Appendix C.**

C. Simulation program

In order to perform the simulations of the $pd \to pnp_{sp}\eta(\eta')$ reactions at the COSY-11 facility a dedicated fast simulation program has been written in FORTRAN '90 language. The fast program allows to avoid a time consuming tracking of the particles through the detection system and instead takes advantage of the acceptance map determined by the full Monte-Carlo program based on the GEANT 3 [46] code. The method reduces the computing time by two orders of magnitude and permits to perform the simulations presented in this thesis within a few days at the available computing power at the COSY-11 experiment.

C.1 Input

The program reads from a special input file reaction charateristics such as for example reaction type, number of events generated[1], beam momentum and its smearing, target position smearing, smearing of outgoing particles momenta, detector geometries and the corresponding angular, momentum and energy resolutions.

C.2 Detector geometry

C.2.1 Spectator detector

The position of the centres of all strips within one module is at first defined in its own frame. Then this position is transformed to the MARS[2] coordinate system via transformation which is simply a superposition of rotation and translation. Parameters of these transformations are defined in the input file.

C.2.2 Neutron detector

The position of centres of each module within the neutron detector is defined directly in the MARS frame.

[1] Where 'number of events generated' means number of *pn* quasi-free collisions. There is no need to produce a certain meson, defined by the reaction type, in every single collision (for instance, the excess energy can be lower than 0).

[2] MAin Reference System frame - a frame, which origin is at the point of the reaction vertex.

C.2.3 Other detectors

The position of other detectors (which influence the COSY-11 acceptance for the reactions under investigation) is defined in the reduced coordinates of beam momentum and read from a second input file. The acceptance of the standard COSY-11 detection system is shown in figure C.1.

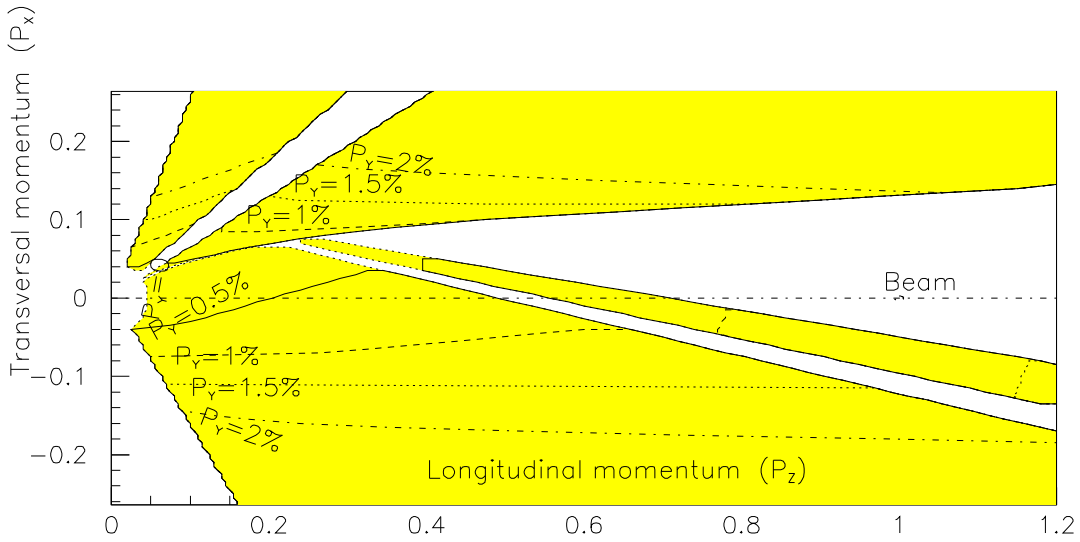

Figure C.1: Acceptance of the COSY-11 standard detection system (drift chambers, silicon monitors, scintillators) for protons. Proton longitudal and transversal momenta are "reduced", i.e. they are given in units of the beam momentum value (see. eq. C.4- C.6).

C.3 Beam momentum

Beam momenta P_x^{beam}, P_y^{beam} and P_z^{beam} are read from the input file. The value of P_z is afterwards being smeared around the main value with a standard deviation $\sigma = 2.0$ MeV/c as determined during the previous COSY-11 experiments [26].

C.4 Target momentum

The spherical coordinates for the momentum of the neutron bound inside a deuteron are calculated. The momentum direction, defined by ϕ and θ angles in the spherical coordinate system, is randomly generated from an uniform distribution on a sphere. Then one of the subprograms calculating the deuteron wave function, mentioned at the end of appendix B is being called in order to generate the absolute value of the neutron momentum (P). Afterwards the momentum vec-

tor is being transformed from spherical coordinates into Cartesian coordinates[3] using the following equations:

$$P_x^{neutron} = P \cdot sin(\theta) \cdot cos(\phi), \tag{C.1}$$

$$P_y^{neutron} = P \cdot sin(\theta) \cdot sin(\phi), \tag{C.2}$$

$$P_z^{neutron} = P \cdot cos(\theta). \tag{C.3}$$

Note that the neutron momentum is naturally smeared and varies from event to event due to the Fermi motion inside the deuteron.

C.5 Reaction vertex

When the `target flag` value in the input file is set to 1, we are dealing with a space-smeared vertex. Otherwise we have got a point-like vertex. The target was assumed to be a vertical cylinder with a diameter of 9 mm [25], which is the average value of the real cluster target diameter used at COSY-11 (see fig. 3.2). The beam smearing in horizontal and vertical direction was assumed to be 2 and 4 mm, respectively[4] [26]. Afterwards, the interaction point is generated at the overlapping region of smeared target and beam.

C.6 Phase space distribution

Having chosen the reaction vertex for the $pn \rightarrow pnX$ reaction the total energy in the proton-neutron center-of-mass system is calculated from the proton beam and neutron target momenta. The total energy in the centre-of-mass of these two colliding particles together with the masses of particles in the outgoing channel are the input variables to the `GENBOD`[5] subroutine, which returns four momenta of all outgoing particles and weights of every single event, denoted as WT. The weights ensure that the momenta are distributed homogeneously in phase space. Four momenta are given in the centre-of-mass frame. The transformation of four-momenta to the LAB system is being done by means of the Lorentz transformation coded in the `cm2lab` subroutine. In such a way we have all initial and final four momenta known as calculated in Monte-Carlo. These values have to be smeared out to take into account the experimental resolution. Smearing procedures will be described later.

[3] In the frame defined in fig. C.1: origin of this frame is at the interaction point between beam proton and target neutron, the z-axis is defined by the beam direction, the x and z-axis define a horizontal plane.

[4] Standart deviations

[5] `GENBOD` subroutine belongs to the standard CERNLIB set of subroutines.

C.7 Acceptance

After the four-momentum vectors for all outgoing particles were determined the program verifies whether the event can be registered by the COSY-11 detection setup. In particular for the reaction $pd \to pnp_{sp}X$ a simultaneous acceptance of the spectator proton, fast proton and neutron is required.

C.7.1 Proton Spectator

It is being checked if the spectator proton reaches the active area of one out of four spectator detector modules. If it happens, the value of a special variable, namely `npixel`**, is set to** 1**.**

C.7.2 Fast proton

For the proton taking part in the $pn \to pnX$ reaction the reduced momenta are calculated:

$$P_x^{p*} = \frac{P_x^p}{P^{beam}}, \tag{C.4}$$

$$P_y^{p*} = \frac{P_y^p}{P^{beam}}, \tag{C.5}$$

$$P_z^{p*} = \frac{P_z^p}{P^{beam}}, \tag{C.6}$$

where $P^{beam} = \sqrt{(P_x^{beam})^2 + (P_y^{beam})^2 + (P_z^{beam})^2}$. Next it is checked whether these reduced momenta belong to the shaded part of fig. C.1, which presents the momentum acceptance of the COSY-11 detection system. If it is fulfilled, the value of `npixel2` **is set to** 1**.**

C.7.3 Neutron

The program checks afterwards whether the neutron reaches the neutron detector region. When it happens the `npixel3` **value is set to** 1**. The probability of detecting a signal in the neutron detector (W_{ND}) is equal to:**

$$W_{ND} = 1 - \exp(\frac{-d}{x_0}) \tag{C.7}$$

where d is the lenght of the neutron trajectory inside the neutron detector, and x_0 is the free path of the neutron inside the neutron detector, which equals 46.4 **cm for the $pd \to pnp_{sp}\eta'$ reaction and** 64.0 **cm for the $pd \to pnp_{sp}\eta$ reaction [47]. This is the way the program takes into account the neutron detector efficiency in drawing up the acceptance spectrum.**

When `npixel · npixel2 · npixel3` $= 1$ **the event is accepted and an histogram of acceptance is being filled with a current value of the excess energy** Q**. New weights**

$$W = WT \cdot W_{ND} \tag{C.8}$$

are used in filling this histogram.

C.8 Missing mass

For the missing mass calculation particle momenta as measured in the experiment have to be used, therefore the program has to smear all Monte-Carlo momenta.

The energy of the spectator proton is smeared with a 40 **keV Gaussian distribution (see. 3.2.2).**

The fast proton momentum is also smeared with a Gaussian distribution [6]**.**

The neutron four-momentum is calculated from the time of flight of the neutron between the reaction vertex and the centre of the module that was hit. A conservative value for time resolution of 0.5 **ns was assumed [36]. The momentum direction is defined by the straight line that connects the point of the reaction vertex and the centre of the hit module.**

All these four-momenta together with smeared beam and target four momenta are used to calculate the missing mass of the meson using eq. 2.1. Missing mass histograms are filled with the weight W defined in equation C.8.

C.9 Estimation of the $pn \to pn\eta(\eta')$ total cross section

In order to estimate the expected rate of the $pd \to pnp_{sp}\eta(\eta')$ **reaction which can be registered per day it is necessary to know not only the detector acceptance but also the cross section for the meson production which depends strongly on the excess energy** Q**.**

[6] Absolute momentum value is smeared with $\sigma = 5$ MeV/c for $pn \to pn\eta$ and $\sigma = 5.5$ MeV/c for the $pn \to pn\eta'$ reaction [48]

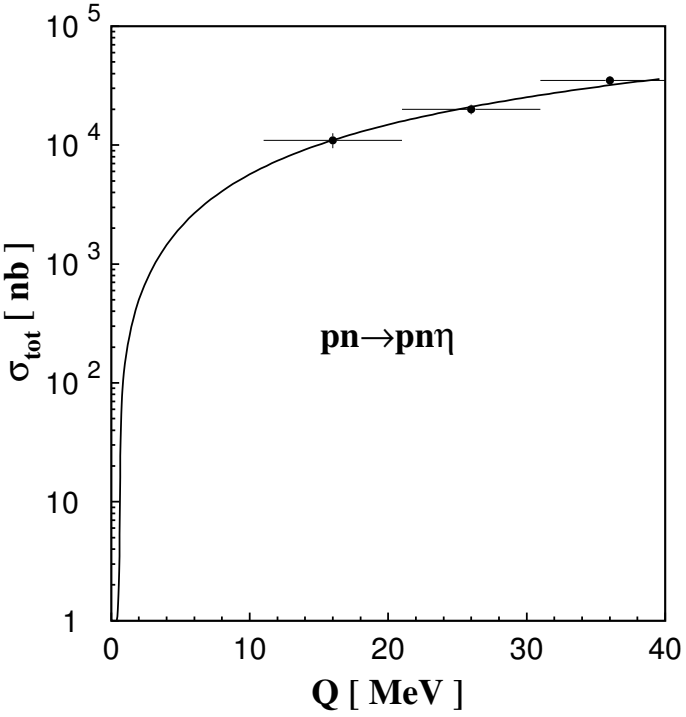

Figure C.2: Parametrization of the total cross section for the $pn \to pn\eta$ reaction. The data are taken from [4].

In order to take this dependence into account new weights W' had to be introduced:

$$W' = W \cdot \sigma, \tag{C.9}$$

where the total cross sections σ have been calculated according to the parametrization for the $pn \to pn\eta$ reaction derived in reference [49] as illustrated in fig. C.2:

$$\sigma^{\eta} = \frac{1}{4} x^{\frac{3}{2}} \sqrt{Q} \frac{1}{(1+\sqrt{1+x})^2} a[1 + \frac{b}{2} Q(1 + \frac{1}{2} \frac{x}{(1+\sqrt{1+x})^2})]. \tag{C.10}$$

In the above equation a dimensionless parameter x has been introduced:

$$x = \frac{Q}{E_B} \tag{C.11}$$

where $E_B = 2.22457$ MeV is the binding energy of the deuteron. The free parameters a and b have been chosen to fit the experimental data in the range from 0 to 40 MeV. Since up to now there is no experimental data concerning the total cross section for the $pn \to pn\eta'$ reaction, it was assumed in the calculations that this total cross section in the frames of the glue excitation model is the same as for a $pp \to pp\eta'$ reaction. For the isovector meson exchange model it was assumed that the total cross section is 6.5 times larger than for the glue excitation model. This assumption is based on a R_η ratio value (see Chapter 1), which is equal to 6.5.

C.10 Proton-neutron final state interaction

The proton-neutron final state interaction is taken into account by weighting the generated events by the square of the proton-neutron elastic scattering amplitude A^2_{pn}. Thus the weight W' of equation C.9 is additionally multiplied by A^2_{pn}:

$$W^{"} = W' \cdot A^2_{pn} \tag{C.12}$$

where A^2_{pn} in the effective range approximation can be expressed as [23]:

$$A^2_{pn} = \frac{1}{p^2_{rel} + (-\frac{1}{a_{np}} + \frac{b_{np} p^2_{rel}}{2})^2}. \tag{C.13}$$

p_{rel} is the momentum of proton or neutron in their own centre-of-mass system:

$$p_{rel} = \frac{\sqrt{\lambda(s_{np}, m^2_p, m^2_n)}}{2\sqrt{s_{np}}} \tag{C.14}$$

where $\lambda(x,y,z) = x^2 + y^2 + z^2 - 2xy - 2yz - 2zx$ and s_{np} is square of the total energy in the $n-p$ centre-of-mass system. In the above equations $a_{np} = -23.74$ fm, $b_{np} = 2.77$ fm denote the scattering length and effective range, respectively [50].

C.11 Output

Finally, as an output the program returns an `.hbook` file, which contains several histograms specific for certain reactions. These `.hbook` files can be afterwards analyzed by means of the PAW analyzing tool [51].

Bibliography

[1] S.D. Bass, e-Print Archive: hep-ph/0006348.

[2] S.D. Bass, Phys. Lett. B 463 (1999) 286.

[3] S.D. Bass, S. Wetzel, W.Weise, Nucl. Phys. A 686 (2001) 429.

[4] H. Calen et al., Phys. Rev. C 58 (1998) 2667.

[5] G.R. Kalbfleisch et al., Phys. Rev. Lett. 12 (1964) 527.

[6] M. Goldberg et al., Phys. Rev. Lett. 12 (1964) 546.

[7] C. Wilkin, e-Print Archive: nucl-th/9810047.

[8] H. Calen et al., Phys. Lett. B 458 (1999) 190.

[9] P. Moskal, T. Johansson, COSY Proposal #100 2001 http://ikpe1101.ikp.kfa-juelich.de/

[10] R. Maier, Nucl. Instr. & Meth. A 390 (1997) 1.

[11] R. Helmer, Can. J. Phys. 65 (1987) 588.

[12] R. Bilger et al., Nucl. Instr. and Meth. A 457 (2001) 64.

[13] S. Häggström, Ph.D. Thesis, Uppsala University (1997).

[14] H. Calen et al., Phys. Rev. Lett. 79 (1997) 2642.

[15] F. Duncan et al., Phys. Rev. Lett. 80 (1998) 4390.

[16] H. Hahn et al., Phys. Rev. Lett. 82 (1999) 2258.

[17] P. Moskal, M. Wolke, A. Khoukaz, W. Oelert, submitted to Prog. Part. & Nucl. Phys. 49 (2002).

[18] D.E. Groom et al., Eur. Phys. J. C 15 (2000) 1.

[19] M. Lacombe et al., Phys. Lett. B 101 (1981) 139.

[20] R. Machleidt, Phys. Rev. C 63 (2001) 024001.

[21] R. Czyżykiewicz, P. Moskal — "Dependence of the excess energy distribution for the quasi-free $pn \to pn\eta'$ reaction on the deuteron wave function model", FZ–Jülich Annual Reports (2002), in press.

[22] E. Chiavassa et al., Phys. Lett. B 337 (1994) 192.

[23] P. Moskal et al., Phys. Lett. B 482 (2000) 356.

[24] S. Brauksiepe et al., Nucl. Instr. & Meth. A 376 (1996) 397.

[25] H. Dombrowski et al. Nucl. Inst. & Meth. A 386 (1997) 228.

[26] P. Moskal et al. Nucl. Inst. & Meth. A 466 (2001) 448.

[27] P. Moskal, Ph.D. Thesis, Jagellonian University of Cracow (1998).

[28] M. Sokołowski et al., Annual Report 1990, IKP, Forschungszentrum Jülich, Germany, Jül-2462 (1991) 219.

[29] M. Wolke, Ph.D. Thesis, Bonn-Universität, Bonn (1998).

[30] Research and Production Association ELMA, Zelenograd, Russia.

[31] Wacker Siltronic AG, Burghausen, Germany.

[32] J. Majewski et al., Annual Reports - Forschungszentrum Jülich, in press.

[33] J. Majewski — private communication.

[34] J. Majewski, E. Białkowski, R. Czyżykiewicz, O. Felden, P. Moskal — "Preparation of silicon pad detectors for measurements of the $pn \to pn\eta$ and $pn \to pn\eta'$ reactions at COSY-11", FZ–Jülich Annual Reports (2002), in press.

[35] Straschu Leiterplatten GMbH 26135 Oldenburg, Germany.

[36] P. Moskal, FZ–Jülich Annual Reports (1996) 35.

[37] E. Byckling, K. Kajantie — "Particle Kinematics", John Wiley & Sons Ltd. (1973).

**[38] H.H. Adam et al., Proceedings of the symposium on threshold meson production in pp and pd interaction, Cracow, June 2001,
Schriften des Forschungszentrums Jülich Reihe: Matter and Materials 11 (2002) 39, in press.**

[39] P. Moskal et al., Phys. Lett. B 517 (2001) 295.

[40] J. Smyrski et al., Phys. Lett. B 474 (2000) 182.

[41] P. Moskal et al., Phys. Lett. B 474 (2000) 416.

[42] A. Bramon, R. Escribano, M.D. Scadron, hep-ph/9711229.

[43] B. Diekmann, Phys. Rep. 159 (1988) 3348.

[44] J.F. Donoghue, H. Gomm, Phys. Lett. B 121 (1983) 49.

[45] F. Lenz, Nucl. Phys. B 279 (1987) 119.

[46] http://wwwinfo.cern.ch/asdoc/geantold/H2GEANTBASE001.html

[47] Th. Blaich et al., Nucl. Instr. & Meth. A 314 (1992) 136.

[48] P. Moskal — private communication (2002).

[49] G. Fäldt, C. Wilkin, Phys. Scripta 64 (2001) 427.

[50] R. Machleidt, I. Slaus, J. Phys. G: Nucl. Part. Phys. 27 (2001) R69.

[51] http://wwwinfo.cern.ch/asd/paw/